A General Filter for Stretched-Grid Models: Application in Two-Dimension Polar Geometry

DORINA SURCEL AND RENÉ LAPRISE

ESCER Centre, Department of Earth and Atmospheric Sciences, Université du Québec à Montréal, Montréal, Québec, Canada

(Manuscript received 5 March 2011, in final form 27 July 2011)

ABSTRACT

Variable-resolution grids are used in global atmospheric models to improve the representation of regional scales over an area of interest: they have reduced computational cost compared to uniform high-resolution grids, and avoid the nesting issues of limited-area models. To address some concerns associated with the stretching and anisotropy of the variable-resolution computational grid, a general convolution filter operator was developed.

The convolution filter that was initially applied in Cartesian geometry in a companion paper is here adapted to cylindrical polar coordinates as an intermediate step toward spherical polar latitude–longitude grids. Both polar grids face the so-called ''pole problem'' because of the convergence of meridians at the poles.

In this work the authors will present some details related to the adaptation of the filter to cylindrical polar coordinates for both uniform as well as stretched grids. The results show that the developed operator is skillful in removing the extraneous fine scales around the pole, with a computational cost smaller than that of common polar filters. The results on a stretched grid for vector and scalar test functions are satisfactory and the filter's response can be optimized for different types of test function and noise one wishes to remove.

1. Introduction

Numerical models have been used for climate modeling for half of a century, and they are powerful tools for reproducing the interactions between different components of the earth's system. Such virtual laboratories would however require computational resources that are not commonly affordable when using high-resolution grids to cover the entire globe for long-term simulations. Two dynamical-downscaling techniques are commonly used by the climate modeling community to reduce the computational costs and achieve high resolution over an area of interest, thus providing potential added value compared with uniform low-resolution global climate models (Solomon 2007).

The first and the most common approach is the one-way nesting of a regional, limited-area model (LAM), which is a noninteractive approach (e.g., Giorgi and Bates 1989; Pielke et al. 1992; Christensen et al. 1998; Caya and Laprise 1999; Wang 2001; Jacob 2001; Döscher et al. 2002; Skamarock and Klemp 2008). LAMs need the specification of time-dependent boundary values that control the regional simulation. Nested models are computationally efficient because of the use of a limited-area domain, but this approach makes achieving an adequate representation of large scales challenging (Fox-Rabinovitz et al. 2008).

A second approach is that of a variable-resolution general circulation model, which consists of using high resolution over a specific region of interest and lower resolution over the rest of the globe, thus naturally allowing two-way interaction between global and regional domains (Fox-Rabinovitz et al. 2008; Laprise 2008). The concentration of resolution over a subset of the earth's surface increases computational efficiency, but this does not come free of some problems owing to the variation of resolution. Variable resolution can be achieved in different ways, but grid stretching is one of the most extensively used methods. Over the last few years the approach of grid stretching in regional climate modeling gained in popularity—for example, the international Stretched-Grid Model Intercomparison Project (SGMIP; Fox-Rabinovitz et al. 2006, 2008) where four major groups from Australia (McGregor and Dix 1997, 2001), France (Déqué and Piedelièvre 1995), Canada (Côté et al. 1997,

Corresponding author address: Dorina Surcel, Centre ESCER, Université du Québec à Montréal, Case postale 8888, Succursale Centre-ville, Montréal QC H3C 3P8, Canada.
E-mail: colan@sca.uqam.ca

DOI: 10.1175/MWR-D-11-00058.1

© 2012 American Meteorological Society

1998), and the United States (Fox-Rabinovitz et al. 1997) evaluated the performance of several stretched-grid general circulation models (SGGCMs) for North American regional climate.

Despite the fact that the variable-resolution approach allows continuous multiyear simulations to be autonomously performed and that provides consistent interactions between global and regional scales of motion, the anisotropy of the grid outside the uniform high-resolution area gives rise to a local degradation in accuracy, which may result in local flow distortions. Surcel and Laprise (2011, hereafter SL11) argued for the benefits of introducing a special filter to remove the modes improperly represented in the stretching areas, thus providing a nearly isotropic and smoothly varying representation on the entire mesh. That filter can be used in the stretching areas of a variable grid as well as to alleviate the ''pole problem'' specific to latitude–longitude grids. The filter can also be applied to control potential numerical instabilities common to all numerical models. The filtering operator is developed using a convolution with a specific weighting function. A key aspect of the proposed approach that makes it particularly suitable to stretched grids is that the weighting function is defined in terms of the physical distance from the application point, rather than gridpoint count. In SL11 the filter was applied in uniform and stretched 1D and 2D Cartesian grids. In this paper we pursue the development of the convolution filter by extending it to cylindrical polar coordinates as an intermediate step toward a spherical polar longitude–latitude grid.

The origin of a polar coordinate system, similarly to the north and south poles on a sphere, constitutes point of convergence for the lines of constant polar angle or constant longitude. This convergence of meridians results in the so-called pole problem with latitude–longitude grids, which imposes severe time-stepping limitations with most numerical schemes. This issue has been circumvented in different ways in the literature such as the use of a ''reduced'' grid in which the longitudinal interval is kept reasonably constant, which can even be beneficial in spectral models (Hortal and Simmons 1991); the filtering of the waves that would become unstable for a chosen time step (e.g., Williamson and Laprise 2000); or applying a polar filter (digital or Fourier) poleward of a specified critical latitude φ_c (typically 45° or 60°), which may be damaging to the accuracy of zonal differencing (Purser 1988).

Usually filters are scaled with grid length rather than physical distance, so their application on anisotropic grids leads to anisotropic damping. The purpose of filtering on a variable grid should be to render the solution effectively isotropic and grid independent. The proposed filter hinges on the fact that the weighting function in the convolution depends on the physical distance rather than on the computational mesh distance, making it particularly suited for stretched grid and polar geometry and for vectors as well as scalars.

This paper is organized as follows. The next section reviews the formulation of the convolution filter in one dimension and presents its adaptation for a polar stretched grid. The third section presents examples of filter application for different scalar tests functions: the filter first is applied on a uniform polar grid to test the control of the pole problem, and then on a variable-resolution polar grid to verify that the filter can remove the noise in the anisotropic region outside the high-resolution area. The fourth section deals with the filtering of vectors. It is shown that the vectors at the points contributing to the convolution need to be expressed in the same reference system. The performance of the convolution operator on vector fields is tested first on a uniform polar grid and then on a variable polar grid. Conclusions are presented in the last section.

2. Description of the convolution filter in polar geometry

Variable-resolution stretched grids usually have uniform high resolution over the area of interest. Outside this area the grid intervals are increased or stretched in one or both horizontal directions, often as a geometric progression with a constant local stretching factor s defined as follows:

$$s = \Delta x_i / \Delta x_{i-1}, \tag{1}$$

where Δx_i and Δx_{i-1} are adjacent grid intervals. The total (or global) stretching factor is defined as

$$S = \Delta x_{\max} / \Delta x_{\min}, \tag{2}$$

where $\Delta x_{\max}$ and $\Delta x_{\min}$ are the maximum and minimum grid intervals over the domain.

A filtering operator is here designed, which aims in part to remove unwanted small scales outside the uniform high-resolution area. The filter is designed around the convolution operator. For a field ψ, the filtered value $\overline{\psi}$ is given by

$$\overline{\psi}(x) = (\psi * w)(x) = \int_{-\infty}^{\infty} \psi(s) w(x - s)\, ds. \tag{3}$$

The spectral response of the convolution is the ratio of the spectral amplitudes, as a function of wavenumbers, of the Fourier transform of the filtered $\overline{\psi}$ and original ψ

fields. SL11 reviewed the well-known mathematical property that the weighting function w in the convolution should be the inverse Fourier transform of the desired response function after the application of the filter, so:

$$w(d) = \frac{1}{2\pi}\int_{-\infty}^{\infty} R(k)\exp(ikd)\,dk.$$

These studies also showed that this formal result could be extended to spatially varying response function and grid mesh, as long as the variations are made gradually. It is thus necessary to first choose a response function and its spatial variation. To prevent the propagation of small-scale signals from the high-resolution region into the regions where the resolution is degraded and the grid anisotropic, we chose a filter operator that will remove the fine scales that are not well represented outside the uniform high-resolution region. The response function is defined as $R(k) = 1$ in the uniform high-resolution region; outside this region we choose

$$R(k) = \begin{cases} 1, & 0 \le k \le a = \pi/\Delta x_{\max} \\ \cos^2\dfrac{\pi}{2}\left(\dfrac{k-a}{b-a}\right), & a < k < b \\ 0, & b \le k \le \pi/\Delta x_{\min} \end{cases}. \quad (4)$$

This function is dependent on the wavenumbers a and b. The parameter a is well determined: $a = \pi/\Delta x_{\max}$. In practice the parameter b is adjusted such as to minimize the Gibbs phenomenon associated with the change of response. The parameters that characterize the convolution can be expressed in term of length scales that must either be retained or removed; therefore $a = 2\pi/L_a$ where L_a is the shortest wavelength that will be entirely preserved and $b = 2\pi/L_b$ where L_b is the longest wavelength that will be completely removed by the filter. Scales with wavelengths between L_a and L_b will be partly damped. Since the response function is even, the inverse Fourier transform that represents the weighting function will be symmetrical with respect to the application point. Hence Eq. (4) then implies that

$$w(x) = \frac{\pi}{2}\frac{\sin ax + \sin bx}{x}\frac{1}{\pi^2 - x^2(b-a)^2}. \quad (5)$$

As shown by SL11, the computational cost can be greatly reduced by truncating the convolution to a user-prescribed finite distance $d_{\max}$ between the application point and the points contributing to the convolution. The resulting filter's response then only approximates the chosen response, but this may often be adequate for practical applications. SL11 presented examples in Cartesian geometry, where for simplicity and computational cost reduction, two-dimensional filtering was obtained by successive applications of one-dimensional filtering in each direction. The study showed that the resulting filter's response was nearly isotropic.

The approach here will be generalized to two-dimensional polar geometry, and the convolution filter will be used in the stretching area and near the pole. In polar coordinates, a point is specified by the radius r, the distance to the origin of the coordinate system, and the azimuthal angle λ. The Cartesian coordinates x and y can be obtained from the relations

$$\begin{cases} x = r\cos\lambda \\ y = r\sin\lambda \end{cases}, \quad \text{where}$$

$$\begin{cases} r = (x^2 + y^2)^{1/2} \\ \lambda = \tan^{-1}\left(\dfrac{y}{x}\right) \end{cases}, \quad 0 \le r < \infty, \quad \text{and} \quad 0 \le \lambda \le 2\pi. \quad (6)$$

We chose a filter formulation obtained by the separate applications of the convolution in the radial and the azimuthal directions, for simplicity and efficiency considerations, while preserving the paramount concept of physical distance. The filtered function can formally be written in integral form as

$$\begin{aligned} \overline{\psi}(r,\lambda) &= \overline{[\overline{(\psi)}^{\lambda}]}^{r}(r,\lambda) \\ &= \int_{r'=0}^{\infty}\int_{\lambda'=0}^{2\pi} \psi(r',\lambda')w[r'(\lambda-\lambda')]w(r-r')r'\,dr'\,d\lambda'. \end{aligned} \quad (7)$$

On a discrete polar grid (r_i, λ_j), fields are represented as $\psi_{i,j} = (r_i, \lambda_j)$, with $i = 1, \ldots, n$; $j = 1, \ldots, m$ and $r_i \in [0, R_e]$, $\lambda_j \in [0, 2\pi)$, where R_e is the distance from the center of the grid to the boundary (henceforth referred to as the equator), and the discrete convolution is as follows:

$$\begin{aligned} \overline{\psi}^{r,\lambda}(r_i,\lambda_j) &= \frac{\sum_k \overline{\psi}^{\lambda}(r_k,\lambda_j)w(d^r_{i-k})s(r_k)}{\sum_k w(d^r_{i-k})s(r_k)} \\ &= \frac{\sum_k\sum_l \psi(r_k,\lambda_l)w(d^{\lambda}_{j-l})w(d^r_{i-k})s(r_k)s(\lambda_l)}{\sum_k\sum_l w(d^{\lambda}_{j-l})w(d^r_{i-k})s(r_k)s(\lambda_l)}, \end{aligned} \quad (8)$$

where d^r_{i-k} and d^{λ}_{j-l} are the radial and azimuthal distances between grid points (r_i, λ_j) and (r_k, λ_l), and $s(r_k)s(\lambda_l) = s(r_k, \lambda_l)$ is the surface area around the (r_k, λ_l) grid point. We stress that the weighting function varies with the physical

distances, and not on gridpoint count, which is in fact the critical ingredient in the design of the proposed filter.

As for the Cartesian coordinate case discussed in SL11, the summation will be truncated to a user-prescribed distance $d_{\max}$ between the application point and the points contributing to the convolution; this will greatly reduce the computational cost when an approximate filter's response suffices. For simplicity and further computational efficiency, the convolution is calculated by successive applications of one-dimensional filtering in each direction. Because the number of grid points for a given physical distance in the azimuthal direction varies with radial distances [in integral Eq. (7) the azimuthally weighting function depends on the radial distance], it is important to first apply the convolution in the azimuthal direction, followed by the application of the convolution in the radial direction. The convolution in the azimuthal direction gives

$$\overline{\psi}^{\lambda}(r_k, \lambda_j) = \frac{\sum\limits_{\substack{l \\ d^{\lambda}_{j-l} \le d_{\max}}} \psi(r_k, \lambda_l) w(d^{\lambda}_{j-l}) s(\lambda_l)}{\sum\limits_{\substack{l \\ d^{\lambda}_{j-l} \le d_{\max}}} w(d^{\lambda}_{j-l}) s(\lambda_l)}, \tag{9}$$

where $d^{\lambda}_{j-l} = r_k(\lambda_j - \lambda_l)$ is the distance between points (r_k, λ_j) and (r_k, λ_l) situated on the same circle r_k = constant, and $s(\lambda_l) = r_k(\lambda_{l+1} - \lambda_{l-1})/2$ is the scale factor in the azimuthal direction corresponding to the grid point (r_k, λ_l). The convolution in the radial direction is calculated as follows

$$\overline{\psi}(r_i, \lambda_j) = \overline{(\overline{\psi}^{\lambda})}^{r}(r_i, \lambda_j) = \frac{\sum\limits_{\substack{k \\ d^{r}_{i-k} \le d_{\max}}} \overline{\psi}^{\lambda}(r_k, \lambda_j) w(d^{r}_{i-k}) s(r_k)}{\sum\limits_{\substack{k \\ d^{r}_{i-k} \le d_{\max}}} w(d^{r}_{i-k}) s(r_k)}, \tag{10}$$

where $d^{r}_{i-k} = r_i - r_k$ is the distance between points (r_k, λ_j) and (r_k, λ_j) situated on the same azimuth λ_j = constant, and $s(r_k) = (r_{k+1} - r_{k-1})/2$ is the scale factor corresponding to the radial direction. Figure 1 shows the grid points participating to the convolutions in the azimuthal and the radial directions.

The computer implementation is greatly simplified by introducing an extended grid for $\lambda < 0$ and $\lambda > 2\pi$. Periodicity considerations give $\psi(r, \lambda) = \psi(r, \lambda \pm 2n\pi)$ with n an integer. Similarly, in order to avoid having to resort to special treatment at the pole and equator, we also use an extension of the physical domain to $r < 0$ and $r > R_e$. For $r < 0$ symmetry of scalars around the pole gives

$$\psi(r, \lambda) = \psi(-r, \lambda \pm \pi). \tag{11}$$

The fields $\psi(r, \lambda)$ are extended for $r > R_e$ by simply using the analytical functions prescribed for our tests. The extension of the domain for $r > R_e$ is only needed because of the polar grid used in this study; on the spherical latitude–longitude grid, this problem does not exist.

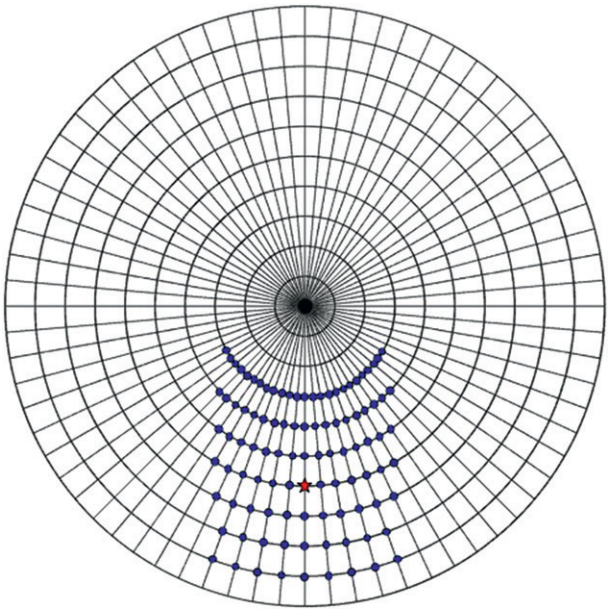

FIG. 1. Simplified sketch showing a typical uniform polar grid. The red star represents the grid point where the filter is applied and the blue circles the grid points contributing to the convolution.

3. Application to scalar fields

By the application of the filter on the polar grid we aim at two objectives: to remove both the pole problem and the anisotropy outside the uniform high-resolution area of the stretched polar grid. We will investigate first the filtering of scalar test functions. The filtering of vector fields will be dealt with in the next section.

For evaluating the skill of the proposed filtering approach, we choose a test function composed of a large-scale field, referred to as the signal or physical component, and a small-scale field, referred to as the noise, defined in every grid point as follows:

$$\psi(r_i, \lambda_j) = \psi_l(r_i, \lambda_j) + \psi_n(r_i, \lambda_j). \tag{12}$$

As in SL11, the quality of the filter will be quantitatively assessed using two metrics: the normalized root-mean-square error (NRMS) and the normalized conservation ratio (NCR). The NRMS will be computed between the filtered solution $\overline{\psi}$ and the expected analytical solution Ψ_l (after subtracting the mean error $\overline{\Delta\Psi}$), normalized by the variance of the analytical solution:

$$\mathrm{NRMS} = \frac{\sqrt{\sum_i \sum_j [\overline{\psi}(r_i, \lambda_j) - \psi_l(r_i, \lambda_j) - \overline{\Delta\Psi}]^2 s(r_i, \lambda_j)}}{\sqrt{\sum_i \sum_j [\psi_l(r_i, \lambda_j)]^2 s(r_i, \lambda_j)}}, \tag{13}$$

where

$$\overline{\Delta\Psi} = \frac{\sum_i \sum_j [\overline{\psi}(r_i, \lambda_j) - \psi_l(r_i, \lambda_j)] s(r_i, \lambda_j)}{\sum_i \sum_j s(r_i, \lambda_j)}$$

is the domain-averaged error between the filtered solution and the analytical solution. The NCR checks mass conservation as the mean error between the filtered and unfiltered solution, normalized by the variance of the analytical solution

$$\mathrm{NCR} = \frac{\sum_i \sum_j [\overline{\psi}(r_i, \lambda_j) - \psi(r_i, \lambda_j)] s(r_i, \lambda_j) \Big/ \sum_i \sum_j s(r_i, \lambda_j)}{\sqrt{\sum_i \sum_j \psi_l^2(r_i, \lambda_j) s(r_i, \lambda_j) \Big/ \sum_i \sum_j s(r_i, \lambda_j)}}. \tag{14}$$

Two types of large-scale signal will be considered:

1) a double cosine in physical space:

$$\psi_l(r_i, \lambda_j) = A_l \cos(k_l r_i \cos\lambda_j) \cos(l_l r_i \sin\lambda_j),$$

where $k_l = l_l = 2\pi/L_l$, L_l (expressed in km) represents the wavelength, and A_l is the amplitude; and

2) a cylindrical harmonic, eigenfunction of the Laplacian on the polar grid:

$$\psi_l(r_i, \lambda_j) = A_l J_{l_l}(k_l r_i) \cos(l_l \lambda_j),$$

where $J_{l_1}(k_l r_i)$ is the Bessel function of the first kind and order l_l (Bowman 1958), k_l is the radial wavenumber, l_l the azimuthal wavenumber, and A_l the amplitude.

The small-scale noise will also be represented by two different test functions:

1) a double cosine in physical space:

$$\psi_n(r_i, \lambda_j) = A_n \cos(k_n r_i \cos\lambda_j) \cos(l_n r_i \sin\lambda_j),$$

where $k_n = l_n = 2\pi/L_n$, L_n (expressed in km) represents the wavelength, and A_n is the amplitude; and

2) a checkerboard-like noise on the polar grid:

$$\psi_n(r_i, \lambda_j) = A_n(\pm 1)^{i+j}.$$

Such noise corresponds to wavenumbers that vary with radial distance, with a minimum value at the equator corresponding to a wavelength of $2\Delta\lambda$.

To avoid difficulties with the extension beyond the artificial boundary of the domain ($r = R_e$) for computer implementation of the convolution, the noise field is gradually diminished to zero over the last four grid points in radial direction.

The weighting function used in the convolution filter formulation represents the inverse Fourier transform of the desired response. It is important to choose a response function with a gradual cutoff, first to minimize the Gibbs phenomena (Sardeshmukh and Hoskins 1984) and second because a smooth cut-off will give rise to a narrower weighting function and the truncation errors related to the application to a finite set of points will be decreased. As we saw in Eq. (5), the parameters that define the weighting function, $a = 2\pi/L_a$ and $b = 2\pi/L_b$, depend on the length scales that a user chooses to preserve or remove. The convolution will be calculated considering all grid points located up to a user-chosen maximum distance $d_{\max}$ in radial or azimuthal directions from the application point.

a. Application to scalars on a uniform polar grid

To test the skill of the filter at alleviating the pole problem, we employ a "uniform" polar grid (i.e., a uniform radial resolution Δr and isotropic resolution near the equator $R_e\Delta\lambda = \Delta r$). With n radial grid points, this implies $n = R_e/\Delta r + 1$ [i.e., $\Delta r = R_e/(n - 1)$ (with grid points both at the pole and the equator)]. With m equally spaced azimuths $\Delta\lambda = 2\pi/m$, this implies $m = 2\pi(n - 1)$ (i.e., $n = m/2\pi + 1$). In the following tests we have used arbitrarily $R_e = 10\,000$ km, the approximate distance between the pole and the equator on earth. To summarize, the discrete uniform polar grid used for our experiments was represented by (r_i, λ_j) with $r_i \in [0, R_e]$ and $i = 1, \ldots, n$ and $\lambda_j \in [0, 2\pi)$, $j = 1, \ldots, m$, and $R_e\Delta\lambda = \Delta r$.

The tests performed on the uniform polar grid, using scalar test functions, were designed to verify the skill of

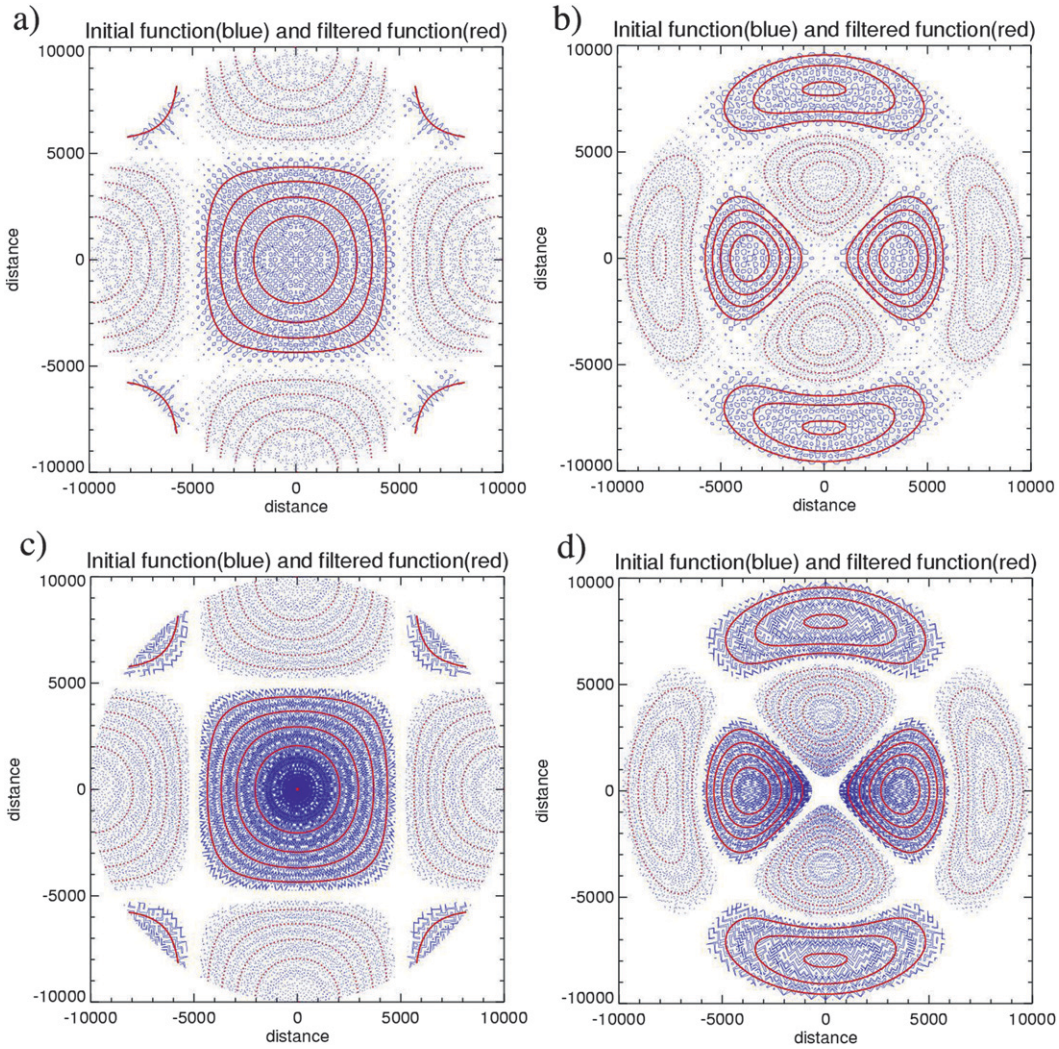

FIG. 2. (a) An initial function shown in blue was composed of a large-scale signal defined as double cosine with L_l = 20 000 km and a small-scale noise in form of a double cosine with L_n = 500 km; the resulting filtered function is represented in red. The weighting function used in the convolution aimed at keeping all waves larger than 2400 km and removing all waves smaller than 800 km. The truncation distance was chosen as $d_{\max}$ = 1600 km. (b) An initial function shown in blue was composed of a large-scale cylindrical harmonic with $k_l = l_l = 2$ and a small-scale noise in the form of a double cosine with L_n = 600 km; the filtered function is represented in red. The weighting function used in the convolution kept all waves larger than 2400 km and removed all waves smaller than 1000 km. The truncation distance was $d_{\max}$ = 2300 km. (c) The initial function is composed from the large-scale signal identical to that used in (a) but with a random noise. The same weighting function and truncation distance as in (a) were used. (d) The initial function is composed from the large-scale signal identical to that used in (b) but with a random noise. The same weighting function and truncation distance as in (b) were used.

the filter at removing the small-scale noise around the pole while preserving the large-scale signal, and to evaluate the influence of using different choices of weighting functions.

For the first objective of handling the pole problem, Fig. 2 presents four examples with different test functions. The uniform polar grid has a resolution of 1° in azimuthal direction, resulting in an isotropic resolution near the equator of $\Delta r \cong 175$ km. In the first example (Fig. 2a), the test function is composed of a large-scale signal in the form of a double cosine with $k_l = l_l = 2\pi/L_l$ and L_l = 20 000 km and a small-scale noise represented also by a double cosine with $k_n = l_n = 2\pi/L_n$ and L_n = 500 km. The amplitude of the large-scale signal is A_j = 1 and that of the noise is $A_n = 1/4$, except for the last four grid points in radial direction where this amplitude is gradually reduced to zero. The parameters of the convolution weighting function were chosen to be

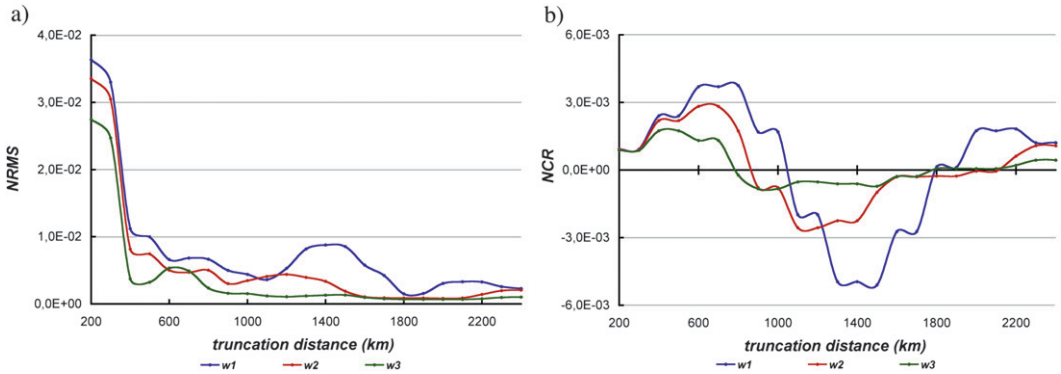

FIG. 3. The (a) NRMS and the (b) NCR scores as a function of the truncation distance for three convolution filters with weighting functions $w_1 : \begin{cases} L_a = 2400 \text{ km} \\ L_b = 1000 \text{ km} \end{cases}$, $w_2 : \begin{cases} L_a = 2400 \text{ km} \\ L_b = 800 \text{ km} \end{cases}$, and $w_3 : \begin{cases} L_a = 2400 \text{ km} \\ L_b = 600 \text{ km} \end{cases}$, applied on the same test function as in Fig. 2a.

L_a = 2400 km and L_b = 800 km, so the filter should preserve the large-scale signal and remove entirely the small-scale noise. With these parameters, the response function is relatively smooth and the weighting function needs a truncation distance of $d_{\max}$ = 1600 km for an adequate accuracy of the convolution. The test function represented in Fig. 2b is composed of a large-scale signal in the form of a cylindrical harmonic with $k_l = l_l = 2$, and a small-scale noise in form of a double cosine with $k_n = l_n = 2\pi/L_n$ and L_n = 600 km. The amplitude of the large-scale signal was set to $A_l = 1$ and, to keep almost the same proportion between the amplitude of the signal and the noise as in the first example, we chose $A_n = 1/8$ except in the last four grid points where the amplitude is diminished gradually to zero. To remove the noise we used a weighting function were L_a = 2400 km and L_b = 1000 km. Because this weighting function has a wider footprint, then an increased truncation distance is necessary for a proper response of the filter, so we chose $d_{\max}$ = 2300 km. The last two examples presented in Figs. 2c,d used test functions composed of large-scale signals identical to those used in the first two examples, but with checkerboard-like noises with amplitudes equal to 1/8 for Fig. 2c and 1/16 for Fig. 2d. To remove these noise patterns the convolution filter employed the same weighting function and truncation distances as in the first two examples. In all four tests shown in Fig. 2, the convolution filter appears to adequately remove the noise and preserve the signal; we will next verify this assessment with a quantitative score.

We now assess quantitatively the influence of the truncation distance and filtering cutoff scale L_b. Three different weighting functions will be tested in the convolution filter applied to the test function used in Fig. 2a. All three weighting functions are designed to remove the noise, as $L_n \leq L_b$, while keeping the large-scale signal; the parameters that characterize these weighting functions are

$$w_1 : \begin{cases} L_a = 2400 \text{ km} \\ L_b = 1000 \text{ km} \end{cases}, \quad w_2 : \begin{cases} L_a = 2400 \text{ km} \\ L_b = 800 \text{ km} \end{cases}, \quad \text{and}$$
$$w_3 : \begin{cases} L_a = 2400 \text{ km} \\ L_b = 600 \text{ km} \end{cases}.$$

Figure 3 shows the curves NRMS and NCR for truncation distances varying between 200 and 2400 km. Figure 3a shows the NRMS for different weighting functions. Overall the error decreases as the truncation distance is increased, although not monotonically; the oscillations are larger for w_1 than for w_3 because of the Gibbs phenomenon associated with a narrower response function, which necessitates a wider stencil for accurate representation. The NCR (Fig. 3b) exhibits important oscillations, even increasing with overly small truncation distance; all curves however eventually asymptote toward zero for large truncation distances, indicating good conservation of filtered quantities at large truncation distances. We note that broader response functions (such as w_3) converge faster because of a reduced spurious Gibbs phenomenon. Beyond a truncation distance of 2400 km the weighting functions become very small and hence their contribution is unimportant in the convolution, and hence NRMS and NCR asymptote toward zero.

We now investigate how the sensitivity to the truncation distance varies depending on the scale of the noise one intends to remove. In Fig. 4 we chose a test function composed of a large-scale signal with $k_l = 2\pi/L_l$

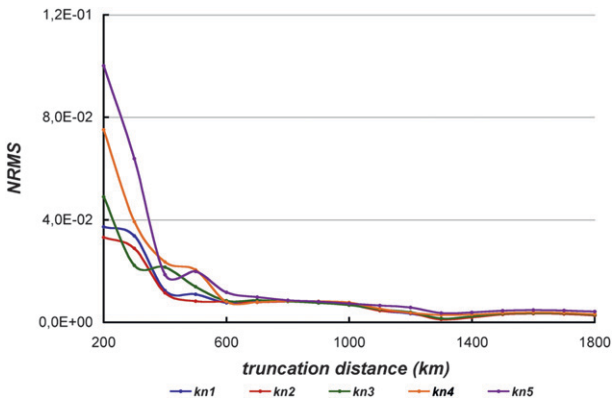

FIG. 4. The NRMS score as a function of the truncation distance when a filter with a weighting function $w: \begin{cases} L_a = 4000 \text{ km} \\ L_b = 1000 \text{ km} \end{cases}$ is applied for five test functions containing a small-scale signal with wavelengths of $L_{n_1} = 500$ km, $L_{n_2} = 600$ km, $L_{n_3} = 700$ km, $L_{n_4} = 800$ km, and $L_{n_5} = 900$ km.

and $L_l = 20\,000$ km and five different double cosine noises with wavenumbers $k_{n_j} = 2\pi/L_{n_j}$ and $(j = 1, \ldots, 5)$, with $L_{n_1} = 500$ km, $L_{n_2} = 600$ km, $L_{n_3} = 700$ km, $L_{n_4} = 800$ km, and $L_{n_5} = 900$ km. We chose a weighting function characterized by

$$w: \begin{cases} L_a = 4000 \text{ km} \\ L_b = 1000 \text{ km} \end{cases},$$

which should be adequate to remove all the above small-scale noises; this weighting function has nonnegligible values over a distance of 1600 km. Figure 4 shows that shorter-scale noises are most effectively removed and they tolerate shorter truncation distance in the convolution filter; as the length scale of the noise increases, convergence is slower and an increased truncation distance is required. However, it can be noted that the error asymptotically converges to zero beyond some truncation distance (in our case 800 km) for all tested noises.

b. Application to scalars on a variable polar grid

We now turn our attention to the application of the filter for removing the anisotropy on a stretched polar grid. We use a uniform high-resolution domain (D_{HR}) defined by

$$D_{\mathrm{HR}}: \left(r, \frac{\lambda}{2\pi}\right) \in (r_1, r_2) \times (t_1, t_2)$$
$$= (3500 \text{ km}; 7500 \text{ km}) \times \left(\frac{5}{8}, \frac{7}{8}\right) \quad \text{with} \quad t_i = \frac{\lambda_i}{2\pi},$$

where the radial resolution is chosen to be $\Delta r \cong 15$ km and the azimuthal resolution $\Delta\lambda \cong \pi/1080$. This implies that resolution will be isotropic in the middle of the high-resolution sector at $[r, \lambda/2\pi] = (5500 \text{ km}; 3/4)$. A gradual stretching zone, with local stretching rate of $s_r = 8\%$ in the radial direction and $s_\lambda = 3.8\%$ in the azimuthal direction, is used adjacent to the high-resolution area, which defines the stretching domain (D_{SG}):

$$D_{\mathrm{HR}} \cup D_{\mathrm{SG}}: \left(r, \frac{\lambda}{2\pi}\right) \in \{(r_3, r_4) \times (0, 1) \cup (0, R_e) \times (t_3, t_4)\}$$
$$= \left\{(2500 \text{ km}; 8500 \text{ km}) \times (0, 1) \cup (0; 10\,000 \text{ km}) \times \left(\frac{9}{16}, \frac{15}{16}\right)\right\}$$

and $D_{\mathrm{HR}} \cap D_{\mathrm{SG}} = \emptyset$.

Low resolution is used elsewhere in the domain, with $\Delta r \cong 90$ km and $\Delta\lambda \cong \pi/180$ (D_{LR}), resulting in a total stretching factor of $S_r \cong S_\lambda \cong 6$.

The test functions used to verify the performance of the filter on variable polar stretched grid are similar to those used for the uniform polar grid. The difference consists in the representation of the small-scale component, which is added in the uniform high-resolution area and in the adjacent stretching regions where the grid is anisotropic. In the uniform high-resolution area (D_{HR}), the small-scale component will be interpreted as part of the signal; it constitutes the added value provided by the stretched grid, and hence the convolution filter will be designed to keep the small-scale component in the uniform high-resolution area. Outside the uniform high-resolution area, the small-scale component will be interpreted as noise that the convolution filter should remove.

The first example is shown in Fig. 5a. The test function is composed of a large-scale double cosine with wavelengths of 20 000 km and a small-scale component in the form of a double cosine with a wavelength of 400 km. The convolution filter uses a weighting function with $L_a = 2400$ km and $L_b = 1000$ km and a truncation distance of 2300 km. Figure 5b shows the filtered function and we can see that the convolution filter adequately removes the finescale noise outside the uniform high-resolution area.

The next example shown in Fig. 5c presents a test function composed of a cylindrical harmonic as large-scale signal and double cosine as small-scale component. The large-scale signal has wavenumbers $k_l = l_l = 2$ and the small-scale component has wavelength of 500 km. The weighting function is characterized by $L_a = 2400$ km, $L_b = 600$ km, and a shorter truncation distance of 1000 km, which is sufficient because of the smoother

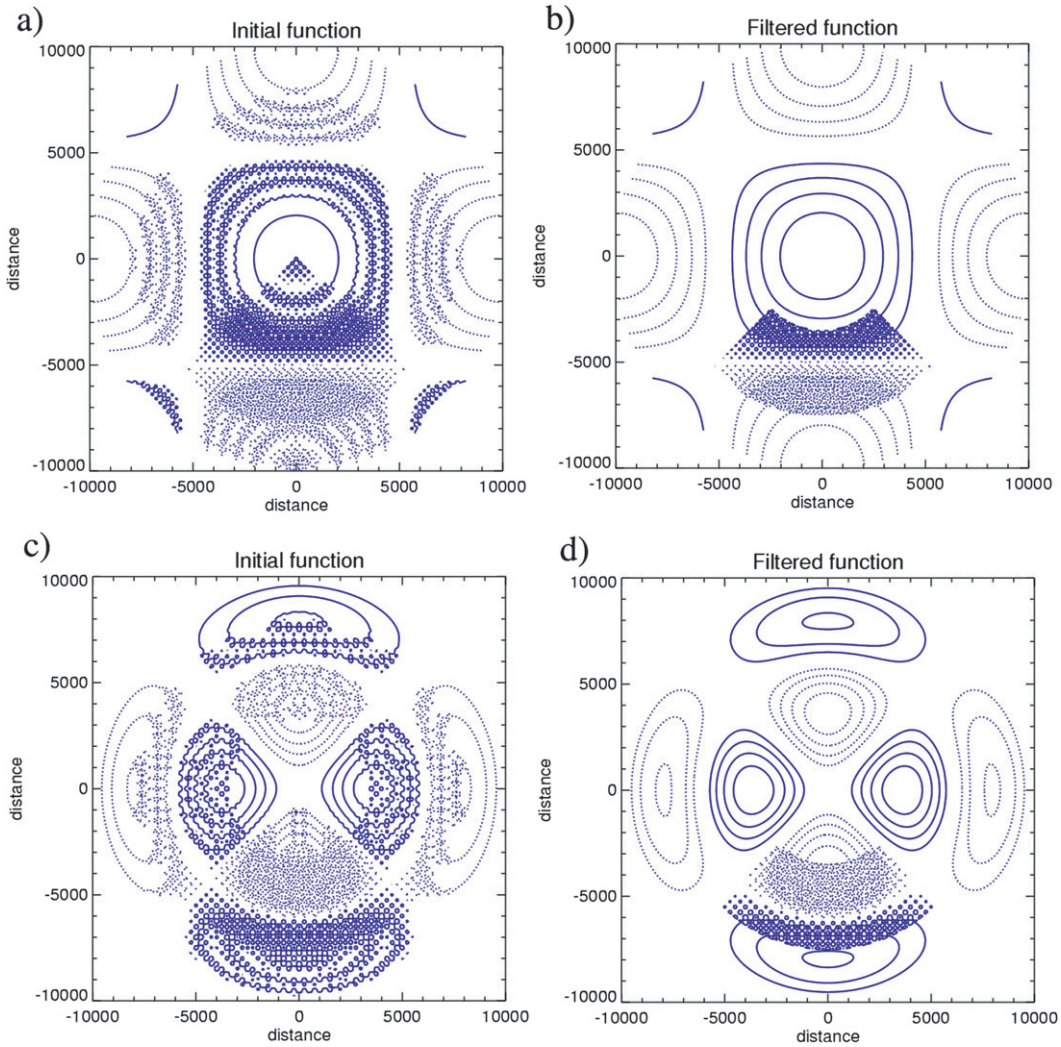

FIG. 5. (a) The test function composed of a large-scale cosine as signal and a small-scale cosine with $L_n = 400$ km as noise is represented on the polar stretched grid with $S_r \cong S_\lambda \cong 6$. (b) The filtered function is obtained using the weighting function $w: \begin{cases} L_a = 2400 \text{ km} \\ L_b = 1000 \text{ km} \end{cases}$ and a truncation distance of 2300 km to remove the noise. (c) The initial test function composed of a large-scale cylindrical harmonic as signal and a small-scale cosine with $L_n = 500$ km as noise is represented on the polar stretched grid with $S_r \cong S_\lambda \cong 6$. (d) The filtered function is obtained using the weighting function $w: \begin{cases} L_a = 2400 \text{ km} \\ L_b = 600 \text{ km} \end{cases}$ and a truncation distance of 1000 km to remove the noise.

response than in the first case, resulting in a narrower footprint of the weighting function. Again we see in Fig. 5d that the convolution filter adequately removes the finescale noise outside the uniform high-resolution area.

We will next quantify the skill of the convolution filter at removing the small-scale noise outside the uniform high-resolution area, while keeping the signal (large and small scales) in the high-resolution area, using similar quantitative scores as for the uniform polar grid. We first establish the following notations:

for the test function

$$\psi(r, \lambda) = \begin{cases} \psi_{\text{HR}} & \text{if} \quad (r, \lambda) \in D_{\text{HR}} \\ \psi_{\text{SG}} & \text{if} \quad (r, \lambda) \in D_{\text{SG}} \\ \psi_{\text{LR}} & \text{if} \quad (r, \lambda) \in D_{\text{LR}} \end{cases},$$

and for the filtered function

$$\overline{\psi}(r, \lambda) = \begin{cases} \psi_{\text{HR}} & \text{if} \quad (r, \lambda) \in D_{\text{HR}} \\ \overline{\psi}_{\text{SG}} & \text{if} \quad (r, \lambda) \in D_{\text{SG}} \\ \overline{\psi}_{\text{LR}} & \text{if} \quad (r, \lambda) \in D_{\text{LR}} \end{cases}.$$

We remark that the convolution filter is applied only outside the uniform high-resolution area, so the filter does not affect the test function in this domain. We consider the analytical solution $\psi_{\rm as}$ as

$$\psi_{\rm as}(r,\lambda) = \begin{cases} \psi_{\rm HR}(r,\lambda) & \text{if} \quad (r,\lambda) \in D_{\rm HR} \\ \psi_l(r,\lambda) & \text{for all other} \quad (r,\lambda) \end{cases}$$

and the NRMS is calculated as

$$\mathrm{NRMS} = \frac{\sqrt{\sum_i \sum_j [\overline{\psi}(r_i,\lambda_j) - \psi_{\rm as}(r_i,\lambda_j) - \overline{\Delta\Psi_{\rm SG}}]^2 s(r_i,\lambda_j)}}{\sqrt{\sum_i \sum_j [\psi_l(r_i,\lambda_j)]^2 s(r_i,\lambda_j)}}, \tag{15}$$

where

$$\overline{\Delta\Psi}_{\rm SG} = \frac{\sum_i \sum_j [\overline{\psi}(r_i,\lambda_j) - \psi_{\rm as}(r_i,\lambda_j)] s(r_i,\lambda_j)}{\sum_i \sum_j s(r_i,\lambda_j)}.$$

We compute similar scores NRMS_SG and NRMS_LR only for parts of the domain; so for the stretching domain $D_{\rm SG}$ and the low-resolution domain $D_{\rm LR}$, we calculate

$$\mathrm{NRMS_}\alpha = \frac{\sqrt{\sum_i \sum_j [\overline{\psi}_\alpha(r_i,\lambda_j) - \psi_{\rm as}(r_i,\lambda_j)]^2 s(r_i,\lambda_j)}}{\sqrt{\sum_i \sum_j [\psi_l(r_i,\lambda_j)]^2 s(r_i,\lambda_j)}}, \tag{16}$$

where

$$\begin{cases} \alpha \equiv \mathrm{SG} & \text{for} \quad (r_i,\lambda_j) \in D_{\rm SG} \\ \alpha \equiv \mathrm{LR} & \text{for} \quad (r_i,\lambda_j) \in D_{\rm LR} \end{cases}. \tag{17}$$

To check the conservation of filtered quantities, NCR is calculated as in Eq. (14).

Three different weighting functions will be applied to the same test function as used in Fig. 5a. By definition, those functions should remove the noise, as $L_n \le L_b$, keeping unchanged the large-scale signal. The parameters characterizing the weighting functions are

$$w_1 : \begin{cases} L_a = 2400 \text{ km} \\ L_b = 1000 \text{ km} \end{cases}, \quad w_2 : \begin{cases} L_a = 2400 \text{ km} \\ L_b = 800 \text{ km} \end{cases}, \quad \text{and}$$

$$w_3 : \begin{cases} L_a = 2400 \text{ km} \\ L_b = 600 \text{ km} \end{cases}.$$

Figure 6a shows that NRMS error generally decreases as the truncation distance increases, although not monotonically. The curves exhibit oscillations that are larger for the weighting function, corresponding to the most abrupt response because of the Gibbs phenomenon. These oscillations are reduced as the truncation distance increases and the error then asymptotes toward zero, as is the case for the weighting function w_3, which only requires a shorter truncation distance in order to reproduce the theoretical spectral response. The conservation scores are shown in Fig. 6b. With sufficiently wide weighting function, NCR eventually approaches zero when using large truncation distance.

The lower two panels in Figs. 6c,d show the normalized error over only the stretching domain (NRMS_SG) and the low-resolution domain (NRMS_LR). The NRMS_SG curves have similar shape as the NRMS curves, which we interpret to imply that the main errors arise from the application of the filter in the stretching region. For a truncation distance smaller than 600 km, NRMS and NRMS_SG generally decrease while NRMS_LR is small, which implies that the convolution filter is effective at removing the noise in the stretching domain. For an increased truncation distance the NRMS error decreases more slowly and the NRMS_LR begins to increase until a value of about 1000 km is reached; this means that the truncation distances smaller than this value are inadequate to reproduce the expected spectral response and that the Gibbs oscillations produce false amplifications or attenuations of the large-scale signal. When the truncation distance is further increased beyond 1000 km, then the error in the low-resolution domain is mostly responsible for the total value of NRMS. All errors decrease toward zero when the truncation distances became large enough to reach vanishing values of the weighting functions.

To substantiate the above interpretation, we will show where in the domain the error occurs using the case already presented in Fig. 5a. The spatial distribution of the quadratic error is computed as the square of the difference between the filtered function and the analytical solution:

$$\sigma^2(r_i,\lambda_j) = [\overline{\psi}(r_i,\lambda_j) - \psi_{\rm as}(r_i,\lambda_j)]^2. \tag{18}$$

Figure 7a shows the quadratic error for a truncation distance of 400 km. We note that the errors are generally located in the stretching zones where some noise remains after the application of the filter. When the truncation distance is increased to 1000 km (Fig. 7b) then the noise remains in the regions where the resolution varies rapidly. When the truncation distance is further increased to 1400 km, then the error is practically removed, but then the Gibbs oscillations give attenuation or amplification of the large scales, resulting in the error pattern shown. The

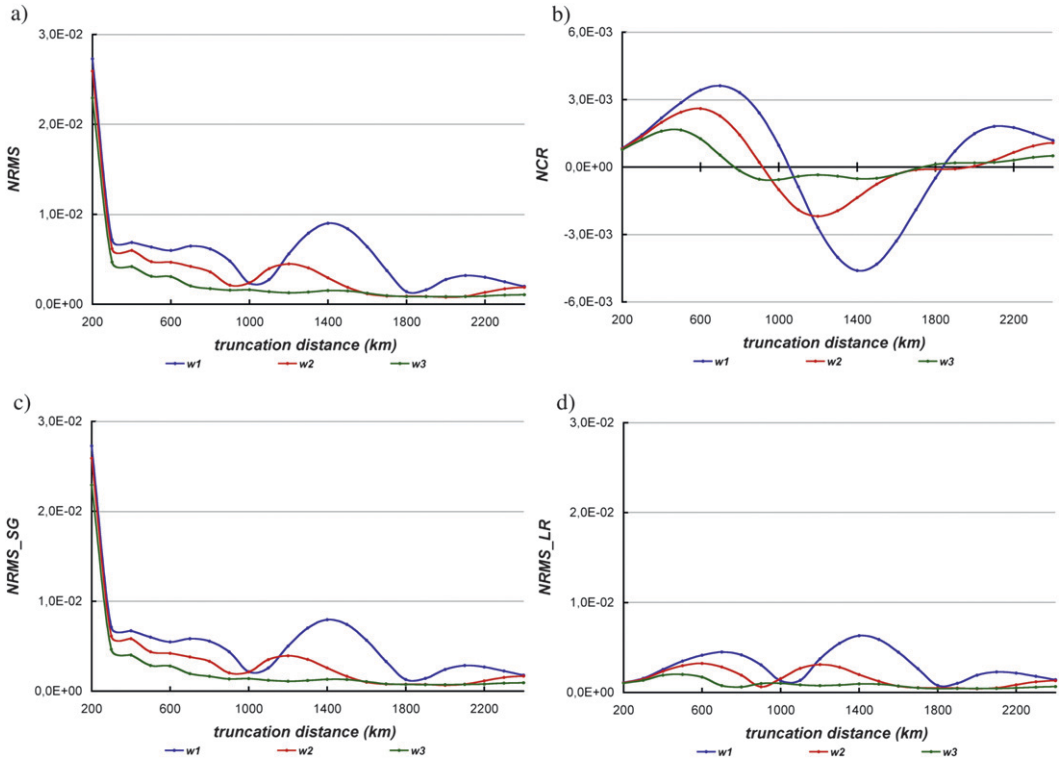

FIG. 6. The (a) NRMS and the (b) NCR scores as a function of the truncation distance for three convolution filters with weighting functions $w_1 : \begin{cases} L_a = 2400 \text{ km} \\ L_b = 1000 \text{ km} \end{cases}$, $w_2 : \begin{cases} L_a = 2400 \text{ km} \\ L_b = 800 \text{ km} \end{cases}$, and $w_3 : \begin{cases} L_a = 2400 \text{ km} \\ L_b = 600 \text{ km} \end{cases}$ applied on the same test function containing a noise with $L_n = 400$ km; (c) the NRMS_SG score is calculated only in the stretching areas; and (d) the NRMS_LR score is calculated in the uniform low-resolution area.

spatial error decreases under the values of 10^{-5} (the minimal value shown in Fig. 7) when the truncation distance exceeds 1800 km.

The experiments realized on the polar grid showed the ability of the convolution filter to adequately remove small-scale noise both in the polar region and also in the anisotropic ''arms-of-the-cross'' regions of the variable polar stretched grid. The convolution filter can be applied at the same time to address the pole problem and also to remove anisotropic noise in the stretching region of the

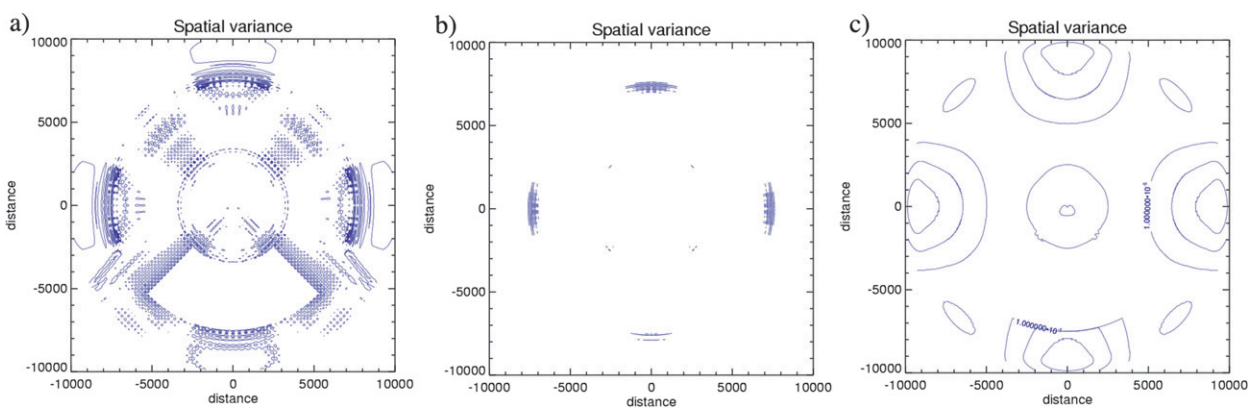

FIG. 7. The spatial distribution of the quadratic error for the same test as that shown in Fig. 5a. The convolution filter used the weighting function $w_1 : \begin{cases} L_a = 2400 \text{ km} \\ L_b = 1000 \text{ km} \end{cases}$. The quadratic error is shown for three different truncation distances of (a) 400, (b) 1000, and (c) 1400 km, respectively.

grid by choosing appropriate parameters for the convolution weighting function. These parameters depend on the length scales that a user wants to be retained or removed in each region of the domain. We reiterate that because the convolution filter is designed in terms of physical distance on the grid and not on gridpoint counts, the resulting response is almost isotropic and independent of gridpoint spacing.

4. Application to vector fields

When the convolution is applied to vectors on a non-Cartesian grid, such as the horizontal winds in spherical polar grid, care has to be taken to use a representation of the vector components relative to the same local reference system. This operation is necessary to account for the effect of the curvature on the sphere and change in the direction of vector basis (Zhang and Rančić 2007). As the polar grid used in this paper is an intermediate step to the application of the filter on a spherical latitude–longitude stretched grid, the representation of the vector components will be made by analogy with the spherical grid. We chose here to express the vectors of the participating grid points in the same local reference system as the point of application of the convolution.

Coordinates on a polar grid are defined by (r, λ), with r the distance from the center of the grid (the equivalent on the sphere would be the radius of the earth multiplied by the colatitude angle) and λ the azimuth angle (equivalent to longitude on the sphere). The horizontal wind is defined related to the local coordinate system, as shown in Fig. 8, with

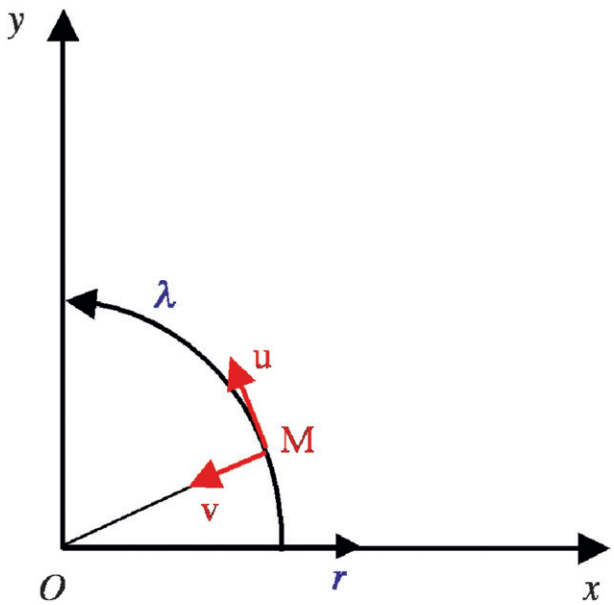

FIG. 8. The representation of horizontal velocity components in polar coordinates.

$$\mathbf{V}_h = (u, v) = \left(r\frac{d\lambda}{dt}, -\frac{dr}{dt}\right),$$

where (u, v) correspond to the "zonal" and "meridional" wind components (using the terminology on the sphere), with the sign convention that u is positive eastward and v is positive northward. Hence the position on the polar grid is defined by (r_i, λ_j) and the horizontal wind components as

$$\begin{cases} u_{i,j} = u(r_i, \lambda_j) \\ v_{i,j} = v(r_i, \lambda_j) \end{cases} \quad \text{with} \quad i = 1, \ldots, n; \quad j = 1, \ldots, m; \quad r_i \in [0, R_e]; \quad \lambda_j \in [0, 2\pi). \tag{19}$$

Following the meteorological tradition, the wind components are defined relative to a locally orthogonal reference system whose base vectors change with location (only with longitude in fact for the polar grid). Therefore the application of the filter operator will require representing the wind components contributing to the convolution at a point in the same coordinate system as that point.

For each point $P_0(r_i, \lambda_j)$ where the convolution filter is applied for (u, v), we need to transform all wind vectors in the neighboring points $P(r_k, \lambda_l)$ contributing to the convolution (i.e., those for which their distance is within the chosen truncation distance for the convolution). The wind components at point $P(r_k, \lambda_l)$ are expressed in the coordinate system relative to the application point P_0 as follows:

$$\begin{pmatrix} u \\ v \end{pmatrix}_{P_0}(k, l) = \begin{bmatrix} \cos(\lambda_l - \lambda_j) & -\sin(\lambda_l - \lambda_j) \\ \sin(\lambda_l - \lambda_j) & \cos(\lambda_l - \lambda_j) \end{bmatrix} \begin{pmatrix} u \\ v \end{pmatrix}_P (k, l). \tag{20}$$

We note that the conversion only involves the longitude angle, not the radial distance, so no transformation is required for points aligned on the same meridian. The equivalent operation on the sphere would consist of projecting the wind vectors of the participating points on the plane that is locally tangent to the application point P_0. We note that there would be alternative approaches on the sphere, such as the Lagrange multipliers (e.g., Côté 1988).

As for scalars, it is convenient to introduce an extended grid that allows applying the general convolution

equation without having to use special treatments near the boundaries of the domain. Hence, if $\lambda < 0$ or $\lambda > 2\pi$, periodicity considerations give

$$\begin{cases} u(r, \lambda) = u(r, \lambda \pm 2n\pi) \\ v(r, \lambda) = v(r, \lambda \pm 2n\pi) \end{cases}$$

with n an integer. Symmetry considerations at the pole suggest the following extrapolation for $r < 0$:

$$\begin{cases} u(r, \lambda) = -u(-r, \lambda \pm \pi) \\ v(r, \lambda) = -v(-r, \lambda \pm \pi) \end{cases}.$$

Again in order to avoid difficulties with the application of the convolution near the artificial boundary of the domain ($r = R_e$), the noise field is gradually diminished to zero over the last four grid points in radial direction.

We define test-wind fields by constructing rotational and divergent motions using the Helmholtz theorem for two-dimensional vector field $\mathbf{V}_h$ as

$$\mathbf{V}_h = \mathbf{V}_R + \mathbf{V}_D = \mathbf{k} \otimes \nabla\psi + \nabla\chi, \tag{21}$$

where ψ is the streamfunction and χ the velocity potential. We then employ test functions similar to those presented in the previous subsection for use as streamfunction or velocity potential, and we develop analytically the corresponding zonal and meridional wind components in polar coordinates. We will use a signal corresponding to either a pure rotational or divergent large-scale motion, and then add to it a small-scale noise that is also either rotational or divergent.

a. Application of the filter for vectors on a uniform polar grid

The filter's ability for application to vectors was tested first on a uniform polar grid. We verified the performance of the convolution filter representing a large-scale wind field, considered as analytical solution; a perturbed wind field, created by adding a noise to the analytic solution; and the filtered wind field, identical with the analytical solution if the filter works properly.

For the first test shown in the Fig. 9, a velocity potential function represented by a double cosine with wavelengths of 20 000 km is used to define a purely divergent large-scale wind field. To this large-scale signal we added a small-scale noise in the form of double cosines with wavelengths of 500 km, either as divergent wind (middle-left panel) or as rotational wind (bottom-left panel). We chose a convolution filter with a weighting function characterized by

$$\begin{cases} L_a = 3000 \text{ km} \\ L_b = 600 \text{ km} \end{cases}$$

and a truncation distance of 900 km. The filtered fields (presented in the right panels of Fig. 9) show that the large-scale signal is preserved and the noise is removed. For this example we used a test field developed analytically from a large-scale double cosine located specifically such as to have nonzero winds at the pole. Numerically the pole is considered as (r_1, λ_j) with $j = 1, \ldots, m$ and the convolution filter is applied there as for all other grid points. The test revealed that the convolution filter works properly in the vicinity of the pole, and the large-scale field is recovered without distortions near the pole.

The next experiment presented in Fig. 10 used a large-scale signal represented by streamfunction in form of a cylindrical harmonic with radial wavenumber $k_l = 1$ and azimuthal wavenumber $l_l = 2$ to show a pure rotational wind field. As before, this large-scale field is perturbed by either a pure divergent or a pure rotational wind noise developed from a small-scale double cosine as velocity potential or streamfunction fields with wavelengths of 500 km. The convolution filter uses a weighting function characterized by

$$\begin{cases} L_a = 3000 \text{ km} \\ L_b = 800 \text{ km} \end{cases}$$

and a truncation distance of 1100 km. Again we note in the right panels that, after the application of the filter, the noise is removed and the filtered fields recover the analytical solution shown in the upper panel.

To quantitatively assess the performance of the filter when is applied for vector fields, we employ the Wind_RMS score calculated as

$$\text{Wind_RMS} = \sqrt{\frac{|\overline{\mathbf{V}} - \mathbf{V}_l|^2}{|\mathbf{V}_l|^2}} = \frac{\sqrt{\sum_i \sum_j \{[\overline{u}(r_i,\lambda_j) - u_l(r_i,\lambda_j)]^2 + [\overline{v}(r_i,\lambda_j) - v_l(r_i,\lambda_j)]^2\} s(r_i,\lambda_j)}}{\sqrt{\sum_i \sum_j \{[u_l(r_i,\lambda_j)]^2 + [v_l(r_i,\lambda_j)]^2\} s(r_i,\lambda_j)}}, \tag{22}$$

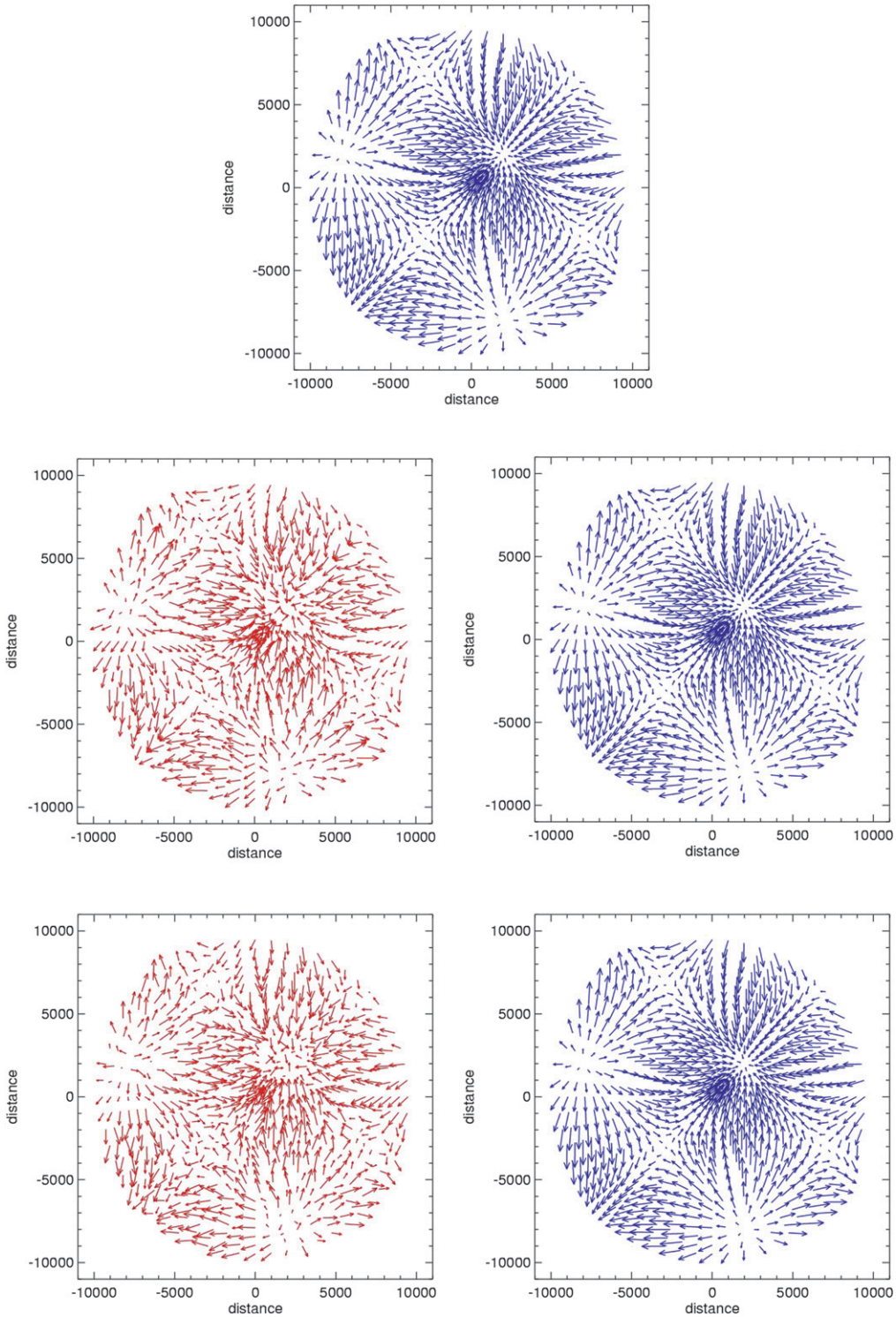

FIG. 9. The (top) large-scale divergent wind field is perturbed by a (middle left) small-scale divergent wind field or by a (bottom left) small-scale rotational wind field. (right) The filtered fields are represented. The large-scale field is built using a scalar cosine function as velocity potential similar to those used when we tested the convolution filter for scalar variables and it has the wavelength $L_l = 20\,000$ km. For both tests, the small-scale field (the noise) was built using cosine scalar functions as velocity potential or streamfunction with $L_n = 500$ km. For all tests, the convolution filter uses the weighting function $w: \begin{cases} L_a = 3000 \text{ km} \\ L_b = 600 \text{ km} \end{cases}$ and a truncation distance of 900 km.

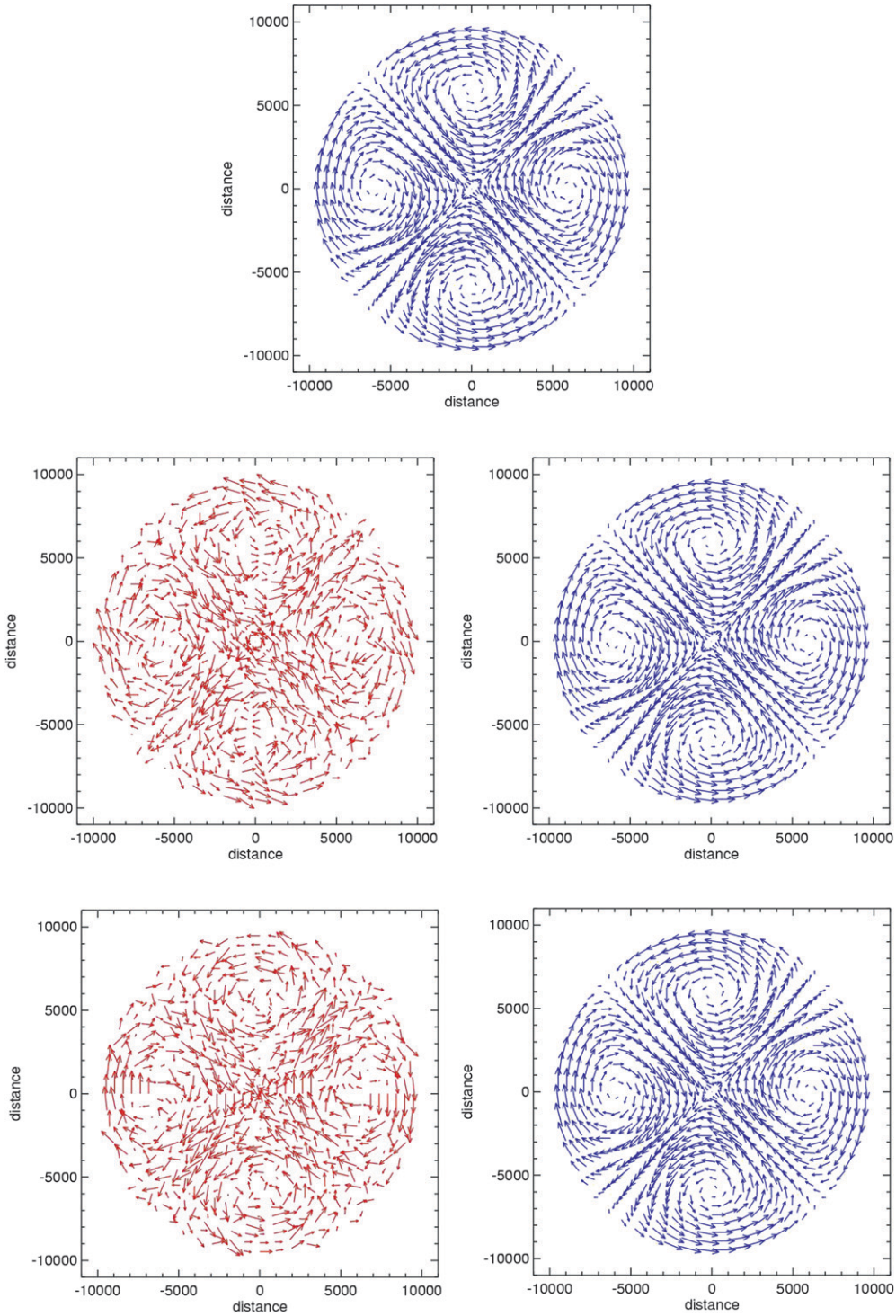

FIG. 10. The (top) large-scale rotational wind field is perturbed by a (middle left) small-scale divergent wind field or by a (bottom left) small-scale rotational wind field. The filtered fields are represented in the right panels. The large-scale field is built using a scalar cylindrical harmonic function as streamfunction similar to those used for scalar variables with wavenumbers $k_l = 1$ and $l_l = 2$. For both tests, the small-scale field (the noise) was built using double cosine scalar functions as velocity potential or streamfunction with $L_n = 500$ km. For the tests presented the convolution filter used the weighting function $w : \begin{cases} L_a = 3000 \text{ km} \\ L_b = 800 \text{ km} \end{cases}$ and a truncation distance of 1100 km.

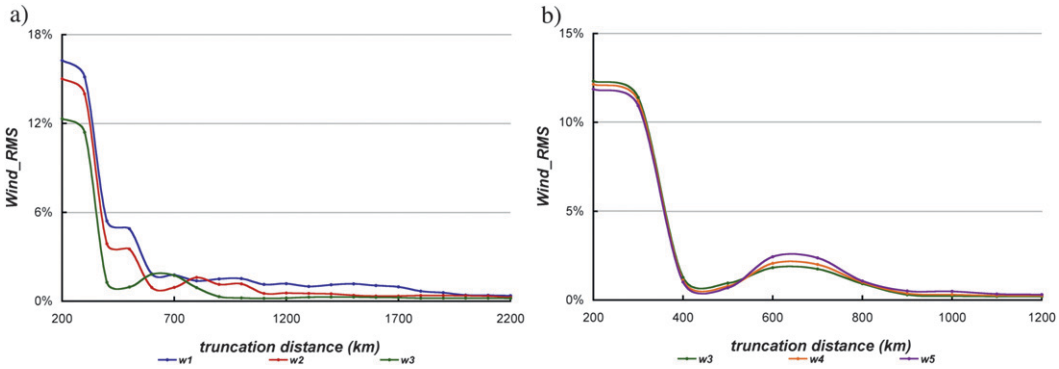

FIG. 11. (a) The Wind_RMS score as a function of the truncation distance for three convolution filters with weighting functions $w_1 : \begin{cases} L_a = 3000 \text{ km} \\ L_b = 1000 \text{ km} \end{cases}$, $w_2 : \begin{cases} L_a = 3000 \text{ km} \\ L_b = 800 \text{ km} \end{cases}$, and $w_3 : \begin{cases} L_a = 3000 \text{ km} \\ L_b = 600 \text{ km} \end{cases}$ applied on the same test function containing a noise with $L_n = 500$ km; (b) the Wind_RMS score as a function of the truncation distance for three convolution filters with weighting functions $w_3 : \begin{cases} L_a = 3000 \text{ km} \\ L_b = 600 \text{ km} \end{cases}$, $w_4 : \begin{cases} L_a = 2600 \text{ km} \\ L_b = 600 \text{ km} \end{cases}$, and $w_5 : \begin{cases} L_a = 2200 \text{ km} \\ L_b = 600 \text{ km} \end{cases}$ applied on the same test function containing a noise with $L_n = 500$ km.

where $\mathbf{V} = \mathbf{V}_l + \mathbf{V}_n$, $\mathbf{V}_l$ represents the large-scale wind vector or the expected analytical solution, $\mathbf{V}_n$ represents the small-scale wind vector or the noise that will be removed, and $\overline{\mathbf{V}}$ is the filtered wind vector solution.

Figure 11 shows the Wind_RMS score as a function of truncation distance for convolution filters using different values of L_a and L_b in the weighting functions. These tests were carried out with a test-wind field composed of a large-scale purely divergent wind with wavelengths of 20 000 km and small-scale rotational noise with wavelengths of 500 km. Figure 11a shows results obtained with various values of L_b, using $L_a = 3000$ km:

$$w_1 : \begin{cases} L_a = 3000 \text{ km} \\ L_b = 1000 \text{ km} \end{cases}, \quad w_2 : \begin{cases} L_a = 3000 \text{ km} \\ L_b = 800 \text{ km} \end{cases}, \quad \text{and}$$
$$w_3 : \begin{cases} L_a = 3000 \text{ km} \\ L_b = 600 \text{ km} \end{cases}.$$

We note that beyond a certain truncation distance, the error is smaller than 0.4% of the error obtained when the truncation distance is very small. As was to be expected the convergence is faster for convolutions with narrower weighting functions such as w_2 and w_3. The next tests shown in Fig. 11b were obtained using $L_b = 600$ km with various values of L_a:

$$w_3 : \begin{cases} L_a = 3000 \text{ km} \\ L_b = 600 \text{ km} \end{cases}, \quad w_4 : \begin{cases} L_a = 2600 \text{ km} \\ L_b = 600 \text{ km} \end{cases}, \quad \text{and}$$
$$w_5 : \begin{cases} L_a = 2200 \text{ km} \\ L_b = 600 \text{ km} \end{cases}.$$

The errors show relative insensitivity to changing L_a. We hypothesize that this reflects the fact that the error also contains a contribution from disturbing the large-scale signal.

To test this hypothesis we compare the performance of filters using the weighting functions w_1 and w_4 that have the same attenuation wavelength bandwidth $L_a - L_b = 2000$ km. Test functions similar to those in the previous tests were used, but with two different large-scale signals characterized by $L_{l_1} = 16\,000$ km and $L_{l_2} = 12\,000$ km, and small-scale noise with $L_n = 500$ km. The resulting Wind_RMS score is represented in Fig. 12. It is evident that w_4 performs better, and both filters are more effective for larger-scale signals $L_{l_1} = 16\,000$ km.

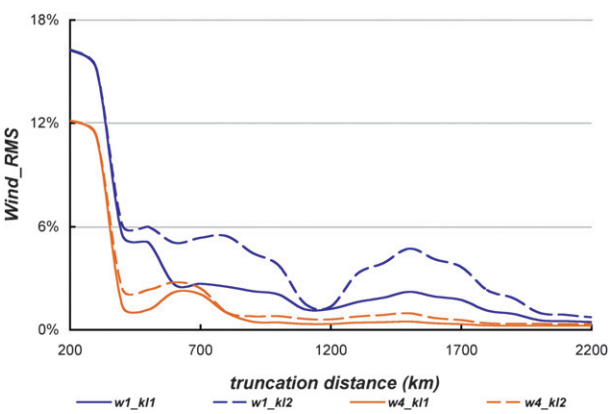

FIG. 12. The Wind_RMS score as a function of the truncation distance for two convolution filters with weighting functions $w_1 : \begin{cases} L_a = 3000 \text{ km} \\ L_b = 1000 \text{ km} \end{cases}$ and $w_4 : \begin{cases} L_a = 2600 \text{ km} \\ L_b = 600 \text{ km} \end{cases}$. The test functions have different large-scale signals with wavelengths $L_{l_1} = 16\,000$ km and $L_{l_2} = 12\,000$ km.

We note that the curves obtained with w_1 weighting function exhibit larger oscillations, but they eventually decrease toward zero for larger truncation distance (around 2200 km).

b. *Application of the filter for vectors on a variable polar grid*

We proceed to tests on a stretched grid, using wind field test functions similar to those used on the uniform polar grid, in order to check the skill of the filter to remove the noise outside of the uniform high-resolution domain. The test functions are composed of a large-scale wind field, which is either purely rotational or purely divergent wind developed analytically from a streamfunction or a velocity potential in the form of double cosines in physical space or cylindrical harmonics, with a wavelength L_l, and a small-scale field that is either rotational or divergent developed similarly to the large-scale field but with wavelength L_n. This small-scale field is gradually added in the stretching zones, where it will be interpreted as noise, and in the uniform high-resolution area where it will be part of the signal and represents the added value of using variable resolution; therefore, in this latter region, the filter will not be applied.

Figure 13 shows a large-scale purely rotational wind field with $L_l = 20\,000$ km (upper panel) perturbed by divergent or rotational small-scale fields (left, middle, and bottom panels) with $L_n = 400$ km. The filter uses a weighting function defined by

$$w: \begin{cases} L_a = 1800 \text{ km} \\ L_b = 600 \text{ km} \end{cases}.$$

and a truncation distance of 1200 km. Because we apply the filter only outside the uniform high-resolution area, and to better display the effect of the filter in the stretching zones, we only present the test function outside the uniform high-resolution zone. Visually we observe that the convolution filter is able to remove the noise, and after the application of the filter, the large-scale signal is recovered. No deformations were noted around the high-resolution domain and the filter works properly in the stretching zones as well as around the pole.

Finally, Fig. 14 shows a purely divergent wind field built from a velocity potential function in the form of a cylindrical harmonic with radial wavenumber 1 and azimuthally wavenumber 2 (upper panel), and perturbed by small-scale fields similar with those used in Fig. 13 using a weighting function with parameters

$$w: \begin{cases} L_a = 1000 \text{ km} \\ L_b = 600 \text{ km} \end{cases}.$$

This weighting function has a broad footprint because it corresponds to a relatively abrupt response function (only 400 km between L_a and L_b) and, for this reason, it needs a truncation distance of 1800 km to remove the noise. The results show suitable performance, with the initial large-scale signal being recovered and no apparent deformations of the wind fields in the stretching regions.

The performance of the filter in removing noise for vector quantities on the stretched polar grid will be quantified using the Wind_RMS score calculated over the entire grid or separately in the stretching zones or the low-resolution region of the domain. If we consider a wind field composed from a large-scale signal and a noise, then we set up the following notations:

for the test field

$$\mathbf{V} = \begin{cases} \mathbf{V}_{\mathrm{HR}} & \text{if} \quad (r, \lambda) \in D_{\mathrm{HR}} \\ \mathbf{V}_{\mathrm{SG}} & \text{if} \quad (r, \lambda) \in D_{\mathrm{SG}} \\ \mathbf{V}_{\mathrm{LR}} & \text{if} \quad (r, \lambda) \in D_{\mathrm{LR}} \end{cases},$$

and for the filtered field

$$\overline{\mathbf{V}} = \begin{cases} \mathbf{V}_{\mathrm{HR}} & \text{if} \quad (r, \lambda) \in D_{\mathrm{HR}} \\ \overline{\mathbf{V}}_{\mathrm{SG}} & \text{if} \quad (r, \lambda) \in D_{\mathrm{SG}} \\ \overline{\mathbf{V}}_{\mathrm{LR}} & \text{if} \quad (r, \lambda) \in D_{\mathrm{LR}} \end{cases}.$$

We computed the Wind_RMS score considering the analytical solution

$$\mathbf{V}_{\mathrm{as}} = (u_{\mathrm{as}}, v_{\mathrm{as}}) = \begin{cases} \mathbf{V}_{\mathrm{HR}} & \text{if} & (r, \lambda) \in D_{\mathrm{HR}} \\ \mathbf{V}_l & \text{for all other} & (r, \lambda) \end{cases}.$$

For the stretched grid, three scores will be calculated. The first score is calculated for the entire domain following the relationship:

$$\text{Wind_RMS} = \sqrt{\frac{|\overline{\mathbf{V}} - \mathbf{V}_{\mathrm{as}}|^2}{|\mathbf{V}_l|^2}} = \frac{\sqrt{\sum_i \sum_j \{[\overline{u}(r_i, \lambda_j) - u_{\mathrm{as}}(r_i, \lambda_j)]^2 + [\overline{v}(r_i, \lambda_j) - v_{\mathrm{as}}(r_i, \lambda_j)]^2\} s(r_i, \lambda_j)}}{\sqrt{\sum_i \sum_j \{[u_l(r_i, \lambda_j)]^2 + [v_l(r_i, \lambda_j)]^2\} s(r_i, \lambda_j)}}$$

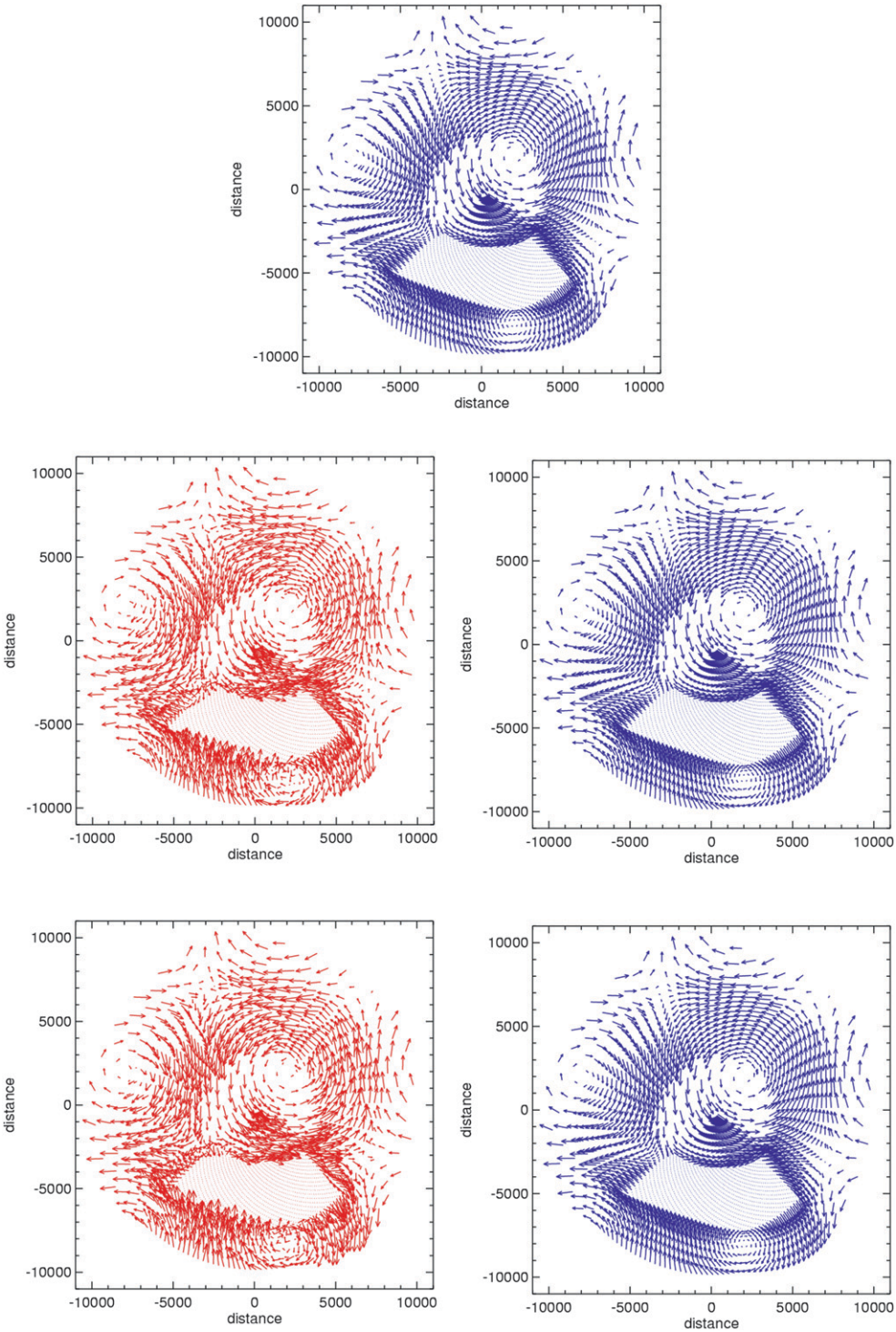

FIG. 13. The (top) large-scale rotational wind field is perturbed by a (middle left) small-scale divergent wind field or by a (bottom left) small-scale rotational wind field. The filtered fields are represented in the right panels. The large-scale field is built using a scalar cosine function as streamfunction similar to those used when we tested the convolution filter for scalar variables. For both test fields the small-scale signal (the noise) was built using cosine scalar functions as velocity potential or streamfunction with $L_n = 400$ km. For the tests presented the convolution filter used the weighting function $w: \begin{cases} L_a = 1800 \text{ km} \\ L_b = 600 \text{ km} \end{cases}$ and a truncation distance of 1200 km. The convolution filter is applied outside the uniform high-resolution area and the test functions are represented only in the regions where the filter is applied.

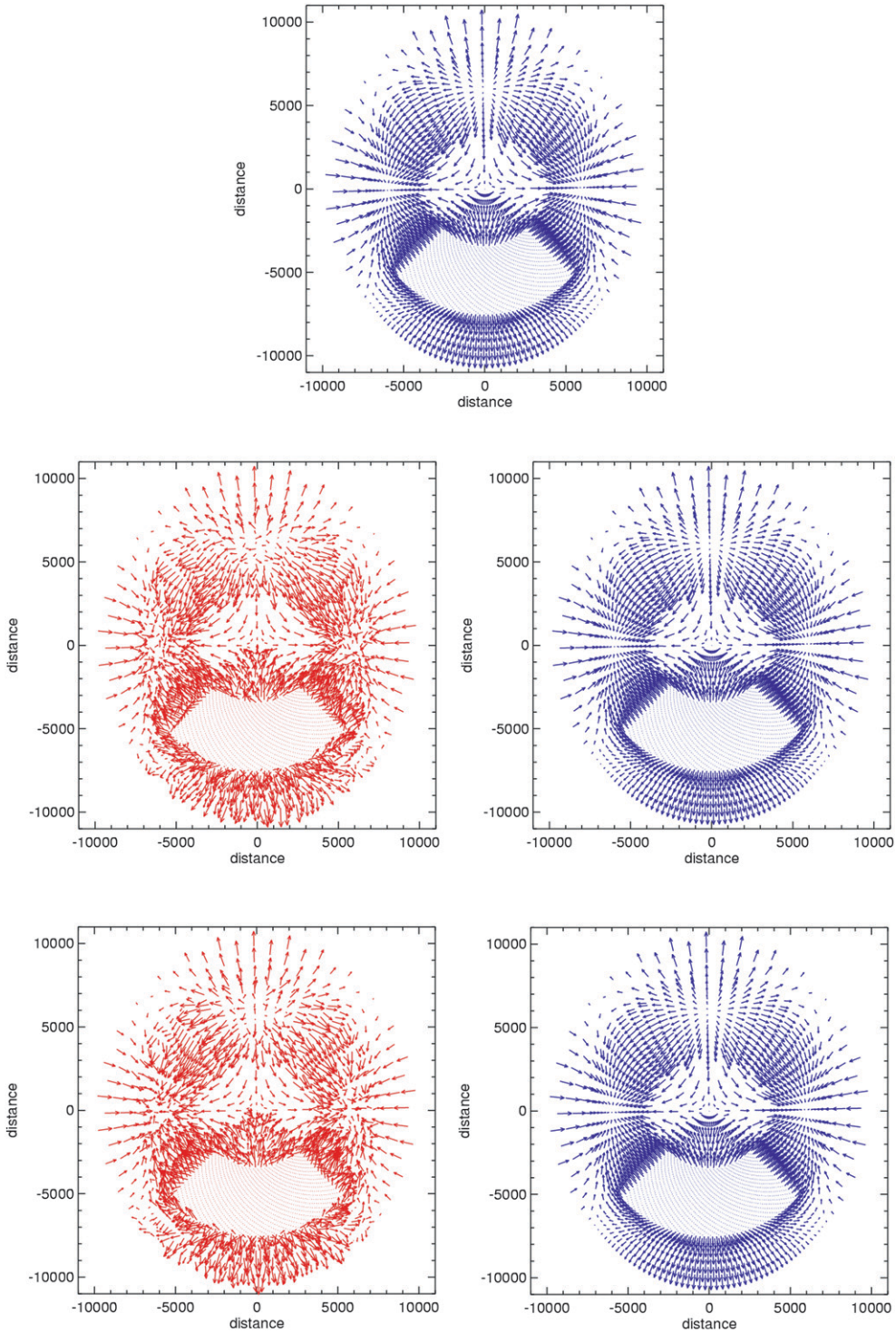

FIG. 14. The (top) large-scale divergent wind field is perturbed by a (middle left) small-scale divergent wind field or by a (bottom left) small-scale rotational wind field. (right) The filtered fields are represented. The large-scale field is built using a scalar cylindrical harmonic function as velocity potential similar to those used when we tested the convolution filter for scalar variables. For both test fields the small-scale signal (the noise) was built using cosine scalar functions as velocity potential or streamfunction with $L_n = 400$ km. For the tests presented the convolution filter used the weighting function $w: \begin{cases} L_a = 1000 \text{ km} \\ L_b = 600 \text{ km} \end{cases}$ and a truncation distance of 1800 km. The convolution filter is applied outside the uniform high-resolution area and the test-functions are represented only in the regions where the filter is applied.

Similarly, we calculate Wind_RMS_SG score for $(r, \lambda) \in D_{SG}$ and Wind_RMS_LR score for $(r, \lambda) \in D_{LR}$.

These tests performed for vectors on the stretched grid used a test-wind field composed of a large-scale purely divergent wind with wavelengths of 20 000 km and a small-scale rotational noise with wavelengths of 400 km. The same three weighting function as for the uniform polar grid were employed, characterized by

$$w_1 : \begin{cases} L_a = 3000 \text{ km} \\ L_b = 1000 \text{ km} \end{cases}, \quad w_2 : \begin{cases} L_a = 3000 \text{ km} \\ L_b = 800 \text{ km} \end{cases}, \quad \text{and}$$

$$w_3 : \begin{cases} L_a = 3000 \text{ km} \\ L_b = 600 \text{ km} \end{cases}.$$

The scores are represented as a function of the truncation distance with values between 200 and 2200 km. The Wind_RMS score for the entire domain is represented in Fig. 15a. We can remark that the error decreases gradually to zero as the truncation distance increases. This error begins to stabilize after 900 km if the weighting function w_3 is used, after 1500 km if the weighting function w_2 is used, and after 2000 km if the weighting function w_1 is used. As is to be expected, the required truncation distance is a function of the width of the weighting function footprint, which is the largest for w_1 and the narrowest for w_3. After the truncation distance reaches large values, the errors decrease to less than 0.4% of the error when the truncation distance is small.

The convolution filter applied on a variable polar grid must remove the noise outside the uniform high-resolution area. The filtering error represents the effect of the filter operator on the signal in the stretching zones and in the uniform low-resolution domain. For this reason we represent the error separately in the stretching domain (the Wind_RMS_SG score) and in the uniform low-resolution domain (the Wind_RMS_LR score). The curve Wind_RMS_SG represented in Fig. 15b has similar shape with the curve Wind_RMS and the errors stabilize after the same truncation distance is reached. This means that the most important part of the error results from the application of the filter in the stretching area. After the stabilization of the error, this is about 0.3% of the error calculated if the truncation distance is small, so we conclude that about 75% of the total error derives from the stretching area. The last curve represented in Fig. 15c shows the effect of the convolution filter on the large-scale signal. Because the small-scale signal is introduced gradually in the stretching domain and in the uniform high-resolution domain, the only signal represented in the low-resolution area is the large-scale one. Inspecting the shape of the Wind_RMS_LR curve, we remark that for

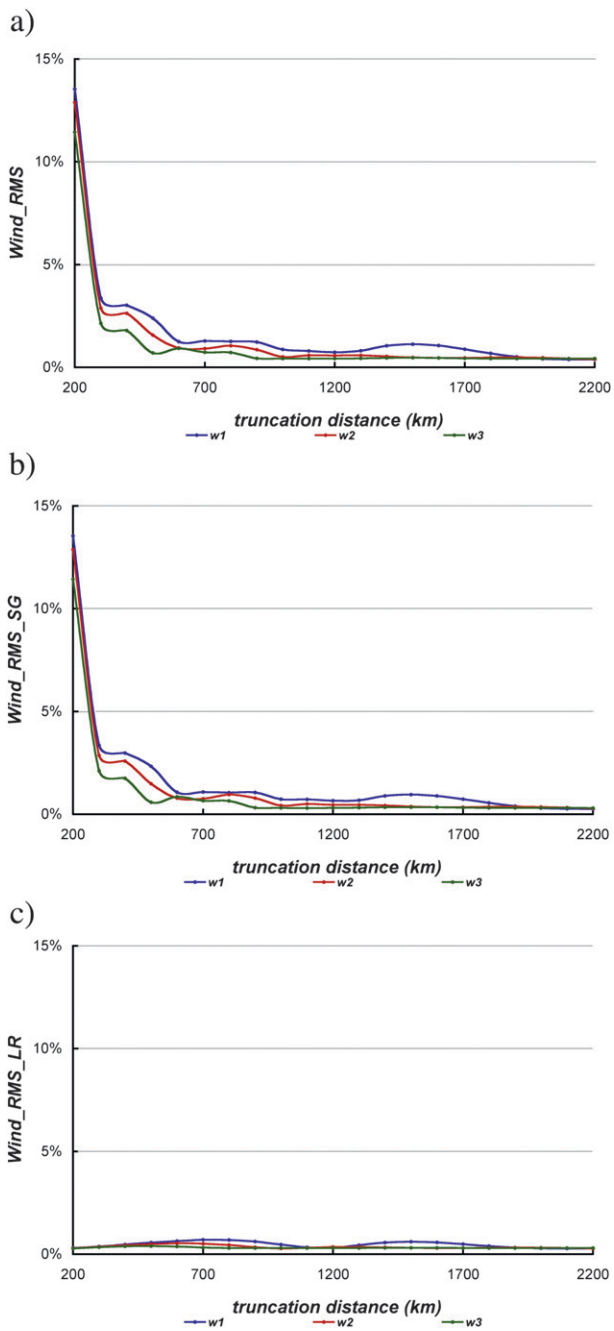

FIG. 15. (a) The Wind_RMS score as a function of the truncation distance for three convolution filters with weighting functions $w_1 : \begin{cases} L_a = 3000 \text{ km} \\ L_b = 1000 \text{ km} \end{cases}$, $w_2 : \begin{cases} L_a = 3000 \text{ km} \\ L_b = 800 \text{ km} \end{cases}$, and $w_3 : \begin{cases} L_a = 3000 \text{ km} \\ L_b = 600 \text{ km} \end{cases}$ applied on the same test function containing a noise with L_n = 400 km; (b) the Wind_RMS_SG score is calculated only in the stretching areas; and (c) the Wind_RMS_LR score is calculated in the uniform low-resolution area.

the weighting function w_3 this is almost flat, meaning that in this case the filter does not affect the large-scale signal. This weighting function has the narrowest footprint corresponding to the smoother spectral response (the attenuation bandwidth is 2400 km). If the attenuation bandwidth is decreased so the spectral response is less smooth, then the weighting function has a larger footprint and it needs a larger truncation distance in order to provide a good filter response. This is demonstrated by the oscillations that appear on the Wind_RMS_LR curve shape for w_2 and w_1. As in the previous cases, the errors stabilize after the same truncation distance is reached. The values of Wind_RMS_LR score are close to zero for large truncation distances, but there is always a small difference of 0.2% from the initial error, which can be explained by unavoidable numerical approximations due to the application of the filter on the variable mesh.

5. Conclusions

The approach of variable resolution has proven to be a viable alternative solution to nested limited-area models for regional climate modeling. Gradually varying resolution of the stretched grid away from the area of interest reduces the computational noise, but it does not resolve the issue of the anisotropy of the grid outside the uniform high-resolution zone.

An adequate filtering technique designed for a variable stretched grid can be a powerful tool to control small scales improperly represented outside the high-resolution region of the zone of interest. The so-called ''arms-of-the-cross'' regions are characterized by differences between gridpoint spacing in latitudinal and longitudinal directions, which may induce all sorts of numerical artifacts as well as make difficult the parameterization of subgrid-scale physical processes.

A convolution filter developed by SL11 was here adapted in this study for polar geometry. The convolution filter uses a weighting function that is the inverse Fourier transform of the desired response function in one dimension. In practice, the convolution can be truncated at some finite distance where the weighting function becomes sufficiently small, which reduces substantially the computational cost, especially in two dimensions. The main distinction of this convolution filter is its formulation based on physical distance rather than on gridpoint distances. Being independent of the underlying grid structure, this filter provides an almost isotropic response, which can conveniently be used to control small-scale noise outside the uniform high-resolution area. The application of this filter for a polar grid can also naturally handle the pole problem characteristic of the latitude–longitude grids.

In the first part of the paper, the mathematical formulation for the convolution filter adapted for 2D polar geometry was described. We found that for application on a polar grid, the 2D convolution could be conveniently cast into the successive applications of 1D convolution in radial and azimuthal directions.

The second part of the paper presented applications in 2D uniform and variable stretched grids. The convolution filter adapted for polar geometry could be applied for scalar variables to resolve the anisotropy of the computational stretched grid or for the pole problem. Choosing cylindrical harmonics or double cosines signals as test functions, we showed that weighting functions could be designed to remove specific noises. This is an important point in the design of this filter operator because it can resolve at the same time both problems mentioned earlier, without the necessity of changing the filter formulation to respond to a certain type of noise. To save on computations, the convolution can be truncated at some finite distance where the weighting function becomes sufficiently small, resulting then in an approximate response. Tests have revealed that the error decreases for larger truncation distances and that the filter conserves approximately the filtered quantities.

It is a common practice to filter the fields (or sometimes their tendencies) in order to remove high wavenumbers that otherwise will affect the accuracy of a climate model. Generally these damping methods are applied to variables such as temperature, pressure, and humidity, and if filtering is needed for momentum, it is generally applied to corresponding scalar quantities such as streamfunction and velocity potential or vorticity and divergence. In our study we proceed to the filtering of the wind vectors themselves. The filter is applied simultaneously for both wind components and the convolution is applied successively in radial and azimuthal directions. With appropriate definition constraints and representing the wind components for all points contributing to the convolution relative to the same reference system as the application point, we were able to remove small-scale noise superimposed on large-scale signals.

In conclusion, the proposed filtering approach appears to be an attractive alternative to a conventional grid point–based smoothing operator for stretched-grid models. Its versatility, applicability for all variables of a model, and filtering for different purposes, such as removing the anisotropy of a variable grid or resolving the pole problem, offers an attractive possibility to adapt this approach for spherical variable-resolution global climate models.

Acknowledgments. This research was done as part of the doctoral project of the first author and as a project

within the Canadian Regional Climate Modelling and Diagnostics (CRCMD) Network, funded by the Canadian Foundation for Climate and Atmospheric Sciences (CFCAS), the Ouranos Consortium for Regional Climatology and Adaptation to Climate Change, and National Centre of Excellence (NCE) Mathematics of Information Technology and Complex Systems (MITACS). Ouranos also provided office space and computational resources during a large part of this work.

REFERENCES

Bowman, F., 1958: *Introduction to Bessel Functions*. Dover Publications, 135 pp.

Caya, D., and R. Laprise, 1999: A semi-Lagrangian semi-implicit regional climate model: The Canadian RCM. *Mon. Wea. Rev.,* **127,** 341–362.

Christensen, O. B., J. H. Christensen, B. Machenhauer, and M. Botzet, 1998: Very high-resolution regional climate simulations over Scandinavia—Present climate. *J. Climate,* **11,** 3204–3229.

Côté, J., 1988: A Lagrange multiplier approach for the metric terms of semi-Lagrangian models on the sphere. *Quart. J. Roy. Meteor. Soc.,* **114,** 1347–1352.

——, S. Gravel, A. Méthot, A. Patoine, M. Roch, and A. Staniforth, 1997: Preliminary results from a dry global variable-resolution primitive equations model. *Numerical Methods in Atmospheric and Oceanic Modelling: The André J. Robert Memorial Volume,* C. Lin, R. Laprise, and H. Richie, Eds., CMOS, 245–259.

——, ——, ——, ——, ——, and ——, 1998: The operational CMC–MRB Global Environmental Multiscale (GEM) model. Part I: Design considerations and formulation. *Mon. Wea. Rev.,* **126,** 1373–1395.

Déqué, M., and J. P. Piedelièvre, 1995: High resolution climate simulation over Europe. *Climate Dyn.,* **11,** 321–339.

Döscher, R., U. Willén, C. Jones, A. Rutgersson, H. E. M. Meier, U. Hansson, and P. Graham, 2002: The development of the coupled ocean-atmosphere model RCAO. *Boreal Environ. Res.,* **7,** 183–192.

Fox-Rabinovitz, M. S., G. L. Stenchikov, M. J. Suarez, and L. L. Takacs, 1997: A finite-difference GCM dynamical core with a variable-resolution stretched grid. *Mon. Wea. Rev.,* **125,** 2943–2968.

——, J. Côté, B. Dugas, M. Déqué, and J. L. McGregor, 2006: Variable resolution General Circulation Models: Stretched-Grid Model Intercomparison Project (SGMIP). *J. Geophys. Res.,* **111,** D16104, doi:10.1029/2005JD006520.

——, ——, ——, ——, ——, and A. Belochitski, 2008: Stretched-Grid Model Intercomparison Project: Decadal regional climate simulations with enhanced variable and uniform-resolution GCMs. *Meteor. Atmos. Phys.,* **100,** 159–177.

Giorgi, F., and G. T. Bates, 1989: The climatological skill of a regional model over complex terrain. *Mon. Wea. Rev.,* **117,** 2325–2347.

Hortal, M., and A. J. Simmons, 1991: Use of reduced Gaussian grids in spectral models. *Mon. Wea. Rev.,* **119,** 1057–1074.

Jacob, D., 2001: A note to the simulation of the annual and interannual variability of the water budget over the Baltic Sea drainage basin. *Meteor. Atmos. Phys.,* **77,** 61–73.

Laprise, R., 2008: Regional climate modelling. *J. Comput. Phys.,* **227,** 3641–3666.

McGregor, J. L., and M. R. Dix, 1997: Development of a global conformal-cubic primitive equations model. Research activities in atmospheric and oceanic modelling 25, World Meteorological Organization Tech. Rep. WMO/TD-792, 3.27–3.28.

——, and ——, 2001: The CSIRO conformal-cubic atmospheric GCM. *IUTAM Symposium on Advances in Mathematical Modelling of Atmosphere and Ocean Dynamics,* P. F. Hodnett, Ed., Kluwer, 197–202.

Pielke, R. A., and Coauthors, 1992: A comprehensive meteorological modeling system—RAMS. *Meteor. Atmos. Phys.,* **49,** 69–91.

Purser, R. J., 1988: Degradation of numerical differencing caused by Fourier filtering at high latitudes. *Mon. Wea. Rev.,* **116,** 1057–1066.

Sardeshmukh, P. D., and B. I. Hoskins, 1984: Spatial smoothing on the sphere. *Mon. Wea. Rev.,* **112,** 2524–2529.

Skamarock, W. C., and J. B. Klemp, 2008: A time-split nonhydrostatic atmospheric model for research and NWP applications. *J. Comput. Phys.,* **227,** 3465–3485.

Solomon, S., D. Qin, M. Manning, M. Marquis, K. Averyt, M. M. B. Tignor, H. L. Miller Jr., and Z. Chen, Eds., 2007: *Climate Change 2007: The Physical Science Basis*. Cambridge University Press, 996 pp.

Surcel, D., and R. Laprise, 2011: A general filter for stretched-grid models: Application in Cartesian geometry. *Mon. Wea. Rev.,* **139,** 1637–1653.

Wang, Y., 2001: An explicit simulation of tropical cyclones with a triply nested movable mesh primitive equation model: TCM3. Part I: Model description and control experiment. *Mon. Wea. Rev.,* **129,** 1370–1394.

Williamson, D., and R. Laprise, 2000: Numerical approximations for global atmospheric general circulation models. *Numerical Modeling of Global Atmosphere in the Climate System,* P. Mote and A. O'Neil, Eds., Kluwer Academic Publishers, 127–219.

Zhang, H., and M. Rančić, 2007: A global Eta model on quasi-uniform grids. *Quart. J. Roy. Meteor. Soc.,* **133,** 517–528.